JOURNAL OF APPLIED CRYSTALLOGRAPHY

ISSN: 1600-5767
journals.iucr.org/j

High-accuracy high-resolution measurements of fluorescence in manganese using extended-range high-energy-resolution fluorescence detection

Daniel Sier, Nicholas T. T. Tran, Tony Kirk, Chanh Q. Tran, J. Frederick W. Mosselmans, Sofia Diaz-Moreno and Christopher T. Chantler

J. Appl. Cryst. (2025). **58**, 42–59

JOURNAL OF APPLIED CRYSTALLOGRAPHY

ISSN 1600-5767

High-accuracy high-resolution measurements of fluorescence in manganese using extended-range high-energy-resolution fluorescence detection

Daniel Sier,[a]* Nicholas T. T. Tran,[a] Tony Kirk,[b] Chanh Q. Tran,[b] J. Frederick W. Mosselmans,[c] Sofia Diaz-Moreno[c] and Christopher T. Chantler[a]*

[a]School of Physics, University of Melbourne, Melbourne, Victoria 3010, Australia, [b]Department of Chemistry and Physics, La Trobe University, La Trobe, Victoria 3086, Australia, and [c]Diamond Light Source, Didcot, Oxfordshire, United Kingdom. *Correspondence e-mail: dsier@student.unimelb.edu.au, chantler@unimelb.edu.au

Received 14 December 2023
Accepted 1 November 2024

Edited by G. J. McIntyre, Australian Nuclear Science and Technology Organisation, Lucas Heights, Australia

Keywords: high-energy-resolution fluorescence detection; HERFD; resonant inelastic X-ray scattering; RIXS; X-ray absorption fine structure; XAFS; extended-range high-energy-resolution fluorescence; XR-HERFD; X-ray emission spectroscopy; XES; manganese; spectral satellites.

The technique of extended-range high-energy-resolution fluorescence detection (XR-HERFD), developed from X-ray absorption spectroscopy, X-ray emission spectroscopy and resonant inelastic X-ray scattering (RIXS), has been used to successfully observe a new X-ray fluorescent satellite in manganese. The experimental methodology, spectral processing and analysis, and how statistical information and structure can be defined, extracted and used from HERFD spectra are detailed. Novel approaches to measure and improve accurate data uncertainty in XR-HERFD, HERFD and RIXS data sets are also presented. This includes definitions of intrinsic resolution and improvements to the resolution of the output and data by a factor of two relative to raw data or standard processing. Novel systematics common in HERFD and RIXS experiments are detailed, including background subtraction and elastic Bragg harmonics, with approaches to dealing with them.

1. Introduction

X-ray spectroscopy is one of the most powerful tools in physics and chemistry for probing complex systems. It has branched from X-ray absorption spectroscopy (XAS) into sub-disciplines of X-ray emission spectroscopy (XES) (Zimmermann *et al.*, 2020) and X-ray absorption fine structure (XAFS) (Newville *et al.*, 1995), which itself contains sub-disciplines including X-ray absorption near-edge structure (XANES) (Bianconi, 1980; Henderson *et al.*, 2014) and extended X-ray absorption fine structure (Gurman, 1995). These techniques are amongst the most popular and commonly used at synchrotrons for local atomic structure determination and analysis.

One of the more recent branches of XAS is resonant inelastic X-ray scattering (RIXS), which is among the most exciting and innovative modern X-ray analysis techniques. Sparks (1974) conducted an experiment on a previously unobserved inelastic scattering process, severely limited in scope and confined to monochromated $K\alpha$ radiation, which is considered to be the first RIXS experiment. The first RIXS experiment using synchrotron radiation followed rapidly (Eisenberger *et al.*, 1976). The technique was used sparingly and evolved over the next decade (Blume, 1985) with increased attention and development into the 1990s (Hämäläinen *et al.*, 1991; Carlisle *et al.*, 1995).

RIXS is very closely related to X-ray resonant Raman scattering or Raman X-ray scattering (Kao *et al.*, 1996), resonant X-ray emission spectroscopy (Glans *et al.*, 1996), and

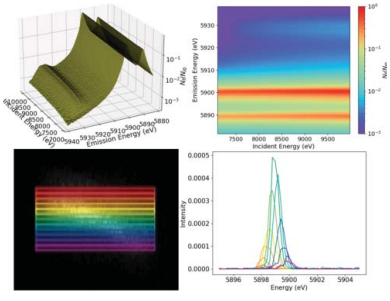

high-energy-resolution fluorescence detection (HERFD) (Hämäläinen *et al.*, 1991; Glatzel & Bergmann, 2005), all of which investigate the energy or momentum transfer of photons over a specific range of incident and emission energies, and most in the vicinity of a resonant transition. These techniques allowed investigations of satellite transition processes (Fritsch *et al.*, 1998), XANES structure (Etalaniemi *et al.*, 1992) and band structure (Carlisle *et al.*, 1995) in new ways that dramatically reduced intrinsic and extrinsic broadening, enabling deeper and clearer insight into the underlying phenomena. Deutsch *et al.* (1996) and Diamant *et al.* (2000) notably investigated HERFD in copper metal in interesting energy regimes. Significant developments were also made in the underlying theory, enabling more information to be extracted from these techniques (Platzman & Isaacs, 1998; Caliebe *et al.*, 1998).

These theories have generally been successful in their comparisons with experimental data and are usually based around the Kramers–Heisenberg formula,

$$I(\Omega,\omega)=\sum_f\left|\sum_n\frac{\langle f|T_2|n\rangle\langle n|T_1|g\rangle}{E_g-E_n+\Omega-i\Gamma_n/2}\right|^2\times\frac{\Gamma_f/2\pi}{\left(E_g-E_f+\Omega-\omega\right)^2+\Gamma_f^2/4},\qquad(1)$$

where $|f\rangle$, $|n\rangle$ and $|g\rangle$ are, respectively, the final, intermediate and ground states. T_1 and T_2 are, respectively, the transition operators between the ground and intermediate and intermediate and final states. Ω and ω are, respectively, the incoming and outgoing X-ray energies. Γ_n and Γ_f are, respectively, the lifetime widths of the intermediate and final states and $E_{f,n,g}$ are the energies of the final, intermediate and ground states, respectively. There are, however, persistent challenges in explaining the presence of Coster–Kronig and radiative Auger transition processes (de Groot, 1996). RIXS now plays a significant role in the study of complex challenges including magnon dispersion, catalysis and high-temperature superconductivity (Braicovich *et al.*, 2009; Timoshenko & Frenkel, 2019; Chen *et al.*, 2011).

X-ray absorption is usually described as a one-electron transition process. However, multiple-electron excitation and ionization are also present and should be observable; these are often described as shake-up and shake-off processes, depending on whether an electron is *excited* to another energy level or *ejected* from the atom, in addition to the regular core electron. These processes result in 'satellite' transitions in which X-rays of higher energy are emitted in comparison with the one-electron $K\alpha_{1,2}$ transitions, and these are observable as asymmetries in the energy distribution. The exact mechanism by which these processes occur is not fully understood (Vatai, 1988; Thomas, 1984). For shake-off processes at high energies, the 'sudden approximation' states that a photoelectron with sufficiently high kinetic energy will leave the atom very quickly, resulting in an abrupt change to the Hamiltonian due to the core hole potential. This implies that the remaining electrons, experiencing this rapidly changing Hamiltonian, have a non-zero probability of also being ejected into the continuum, resulting in a multi-electron excitation (Roy *et al.*, 2001).

The science and detection of these processes require development of the standard HERFD techniques into extended-range HERFD (XR-HERFD), which we describe herein. This paper discusses XR-HERFD experiments and the different types of measurement scan, explains the basis of XR-HERFD, the details of data processing and how to estimate HERFD and RIXS precision and uncertainty, and expands on the technique of pooling multiple data sets and the separation of signals (Hayashi *et al.*, 2004; Hayashi, 2008; Moretti Sala *et al.*, 2018) to increase resolution and sensitivity, with discussions of systematics, noise and statistics. Our purpose in this paper is to develop and define robust accurate techniques and thereby find new insight into satellite structure (Sier *et al.*, 2024) and science using HERFD, RIXS and XR-HERFD.

2. Experimental details

2.1. Beamline

Data were collected at Diamond Light Source on the I20-Scanning beamline (Fig. 1) (Diaz-Moreno *et al.*, 2009; Diaz-Moreno *et al.*, 2018). The setup includes water-cooled rhodium and silicon striped collimating and deflection mirrors to maximize flux and tune the vertical divergence from the wiggler source to the four-bounce monochromator, which consists of two pairs of counter-rotating cryogenically cooled Si(111) crystals in a (+ − − +) configuration. The energy resolution is then determined primarily by the intrinsic energy resolution of the crystals, and the divergence of the incoming beam will not affect the energy of the monochromated beam. This is a fixed-exit geometry, so the position of the monochromatic beam is stable with energy, independent of the source angular position. The instrument also suppresses the reflectivity curve tails (Hayama *et al.*, 2018). After the monochromator there are two more vertically deflecting mirrors to focus the X-ray beam in both the horizontal and vertical planes, and this can achieve a FWHM of 300 × 400 µm at the sample. This focusing may then introduce divergence. These mirrors are followed by two rhodium and silicon striped harmonic rejection mirrors used to remove higher harmonics from the beam below 18 keV (Fig. 1). There is a 15 cm long ion chamber filled to 1800 mbar with a mixture of Ar and He, 1 m upstream of the sample, monitoring the incident beam intensity.

The X-ray emission spectrometer follows a 1 m diameter Rowland circle working in the vertical plane in Johann configuration. To investigate the Mn $K\alpha$ emission spectral region, this was equipped with three spherically bent germanium analyser crystals of 100 mm diameter which focus onto the pixel detector (Diaz-Moreno *et al.*, 2009; Diaz-Moreno *et al.*, 2018; Hayama *et al.*, 2021). The analyser crystals were masked such that only X-rays from the central 50 mm radius were seen, making a nearly ideal Rowland circle geometry and image focus.

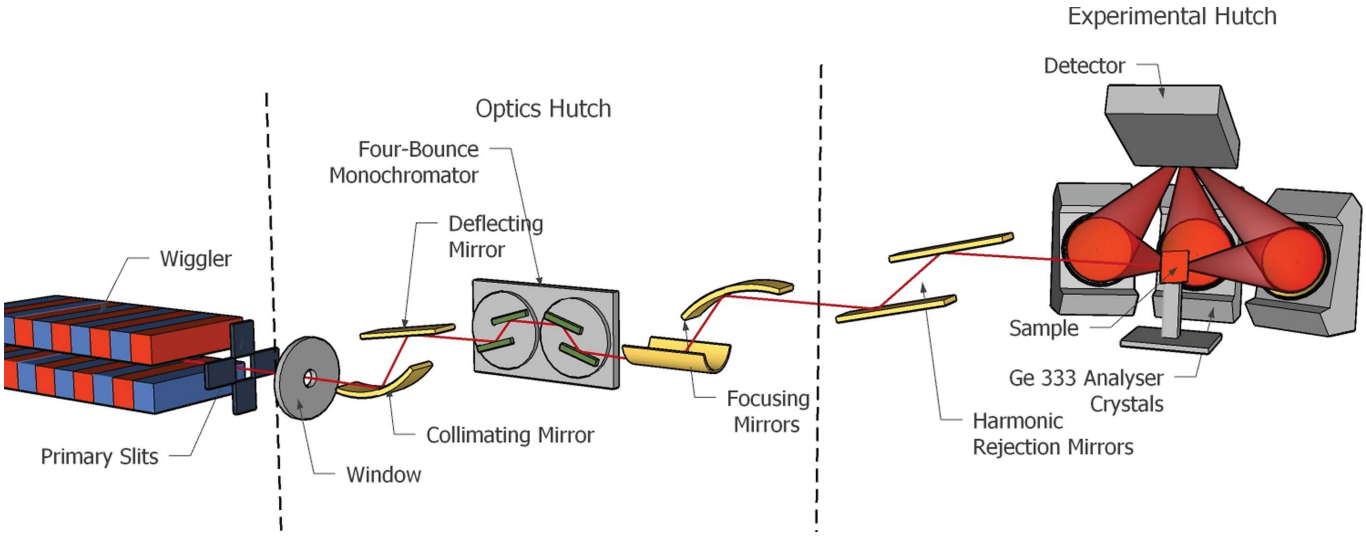

Figure 1
A schematic diagram of the I20-Scanning beamline in XES mode. X-rays delivered by the wiggler source are vertically collimated by a mirror, monochromated by a four-bounce monochromator, and focused horizontally and vertically by the focusing mirrors. Photons emitted from the sample are diffracted by a set of three Ge(333) curved analyser crystals before being collected on a spatially resolving detector, the sensitive face of which is on the far side as viewed in the figure.

2.2. Detector

In order to collect low-intensity satellite transition photons with sufficient statistics, and to distinguish them from the diagram transitions, a high-sensitivity high-resolution spectrometer was used.

This experiment used a MAXIPIX (multichip area X-ray detector based on a photon-counting pixel array) TAA22PC detector which is a development of the Medipix2 single photon counting pixel detector (Llopart *et al.*, 2001; Ponchut *et al.*, 2011). This enables profound advantages in spatial resolution over alternative detectors such as silicon drift detectors, scintillators and ion chambers, as well as a high readout speed, no noise, no dark current, a large dynamic scale and energy discrimination. As we will discuss later, the spatial resolution enables in particular significant improvements in resolution through post-processing techniques, making this an ideal detector for this experimental technique. This experiment utilized a 4×1 detector arrangement giving a 1024×256 effective pixel grid (Fig. 2).

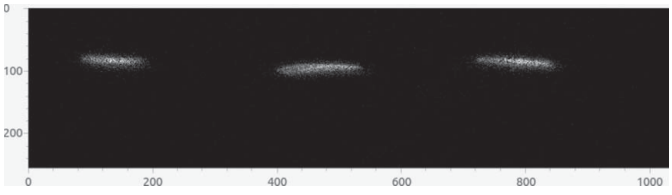

Figure 2
A MAXIPIX detector image with each of the three individual Ge analyser crystal images visible, representing the intensity of one specific fluorescent energy to which the crystals have been tuned, arising from excitations from a particular incident energy from the four-bounce monochromator. We discuss in later sections how the deliberate separation of analyser crystal images enhances resolution, statistics, redundancy and calibration.

2.3. Samples and alignment

These experiments focused specifically on manganese metal. The pure Mn sample was a 25 µm thick foil from Goodfellows. The samples were mounted 45° relative to the incident beam and hence 45° relative to the central crystal analyser of the spectrometer.

2.4. Different scans and their purposes

There are a number of different types of scan on any HERFD or RIXS beamline:

(i) Elastic scan (1D) [Fig. 3(*a*)]. An elastic scan fixes the incident beam energy at a specific value and measures the fluorescence (Rayleigh scattered photons) across a range of different emission energies. It is often performed on the plastic side of the sample mount or on a polymer with strong scatter. If a foil is used, then it is performed below the $K\alpha_1$ fluorescence line and the only emitted energy is the incident elastically scattered energy. If the scan is done on plastic or polymer, the incident energy is chosen to be close to the fluorescence line of interest for the study.

(ii) HERFD-XES (1D) [Fig. 3(*b*)]. This involves fixing the incident energy to a specific value, usually just above the absorption edge for maximum statistics, and collecting the emission spectra using the curved analyser crystals. This investigates the emission spectra.

(iii) XANES, XAFS or XAS scans (fluorescence detection) (1D) [Fig. 3(*c*)]. On a conventional beamline, it is very common to collect a XANES, or in general an 'XAS spectrum', as a 1D scan. In this case, the detector will measure all radiation lost to the beam; in fluorescence, the detector will measure either all radiation scattered at the detector angle to the beam or a region of interest set to follow the dominant fluorescence spectrum of interest. This differs from regular

XES, where the incident energy is usually not fixed to a specific value and which has a much lower resolution.

(iv) HERFD-XANES, HERFD-XAFS or HERFD-XAS (1D) [Fig. 3(*c*)]. The 1D scans analogous to XANES, XAFS or XAS are HERFD-XANES, HERFD-XAFS or HERFD-XAS scans, respectively. In these cases, the analyser crystal energy or angle is fixed to an arbitrary angle or energy. This is usually the peak of the spectrum of interest for the best statistics or alignment, but the energy can be fixed to an alternative energy. With HERFD, this has the benefit of reducing broadening (Kowalska *et al.*, 2016) at the cost of lower flux and statistics, and can filter out signal from undesired edges. A scan is typically classified as 'HERFD' if the energy resolution detection function has a bandwidth similar to or less than the core hole lifetime broadening of the transition of interest. It also allows for investigation of specific areas of the emission spectrum and, importantly, on its own is a different theoretical object from the corresponding XANES, XAFS or XAS scans.

(v) RIXS (2D) [Fig. 3(*d*)]. This 2D map is usually in the bound–bound (resonant) region of the spectrum, that is, the pre-edge and edge region, and potentially in the first few oscillations of the XANES region. It involves gradually increasing the incident energy while also scanning over the emission spectrum. On I20-Scanning, the emission energy will be held constant while the incident energy is stepped over the desired range, typically the XANES, pre-edge or bound–bound regions, after which the emission energy will be incremented and the incident energy will be stepped over again. This is done as it is typically much faster to adjust the incident energy accurately via the four-bounce monochromator than via the analyser crystals. This results in a 2D map as shown in Fig. 4.

(vi) XR-HERFD (2D) (Fig. 5). The most complex of the maps we introduce and define here is that corresponding to XR-HERFD (Tran *et al.*, 2023; Sier *et al.*, 2024). This scan is similar to a RIXS or HERFD scan, where both the incident

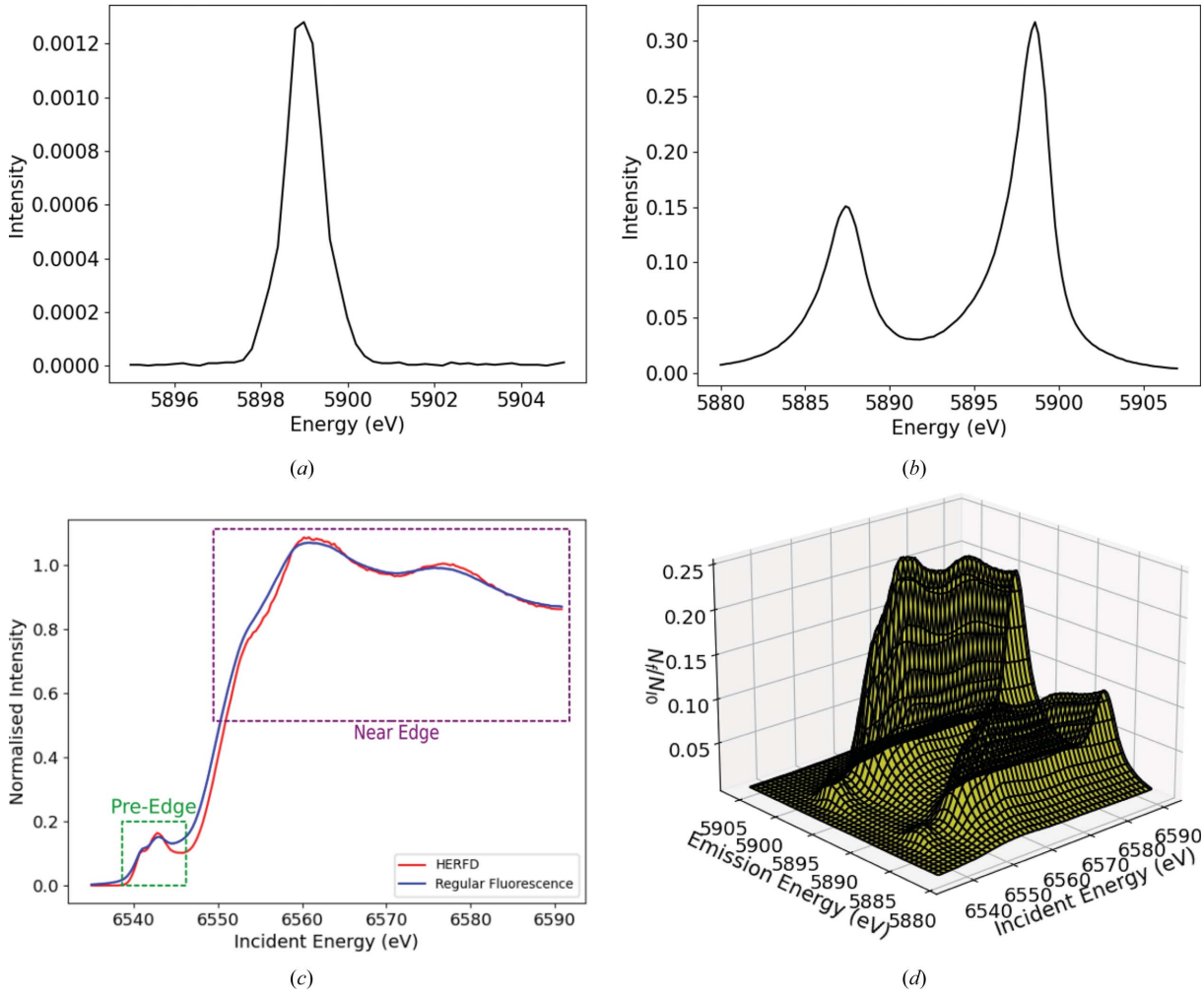

Figure 3
Integrated counts on the detector normalized by the incident counts in different scan types. (*a*) An elastic scan, HERFD-XES, E_{incident} fixed. Often E_{incident}, $E_{\text{emission}} < E_{\text{fluorescence}}$, E_{edge} (the incident beam is often incident upon the plastic mount side of the sample or a polymer with good scatter, and often at an energy close to the fluorescence line). (*b*) An HERFD-XES scan, E_{incident} fixed. $E_{\text{incident}} > E_{\text{edge}}$, showing the characteristic spectrum of *e.g.* MnO $K\alpha_{1,2}$. (*c*) An HERFD-XANES scan of the *K* edge of MnO_2, E_{emission} fixed, usually E_{emission} = maximum of the selected emission line. $E_{\text{incident}} > E_{\text{pre-edge minimum}}$, a scan across the XANES region. Indicated in red is the corresponding integral along the XES axis of a 2D HERFD scan, simulating the lower resolution of a standard XANES scan. (*d*) A 2D scan (3D plot) RIXS map, showing pre-edge and near-edge structure and complexity, in this case for MnO_2. Hereinafter E_{incident} is denoted by E_{i}.

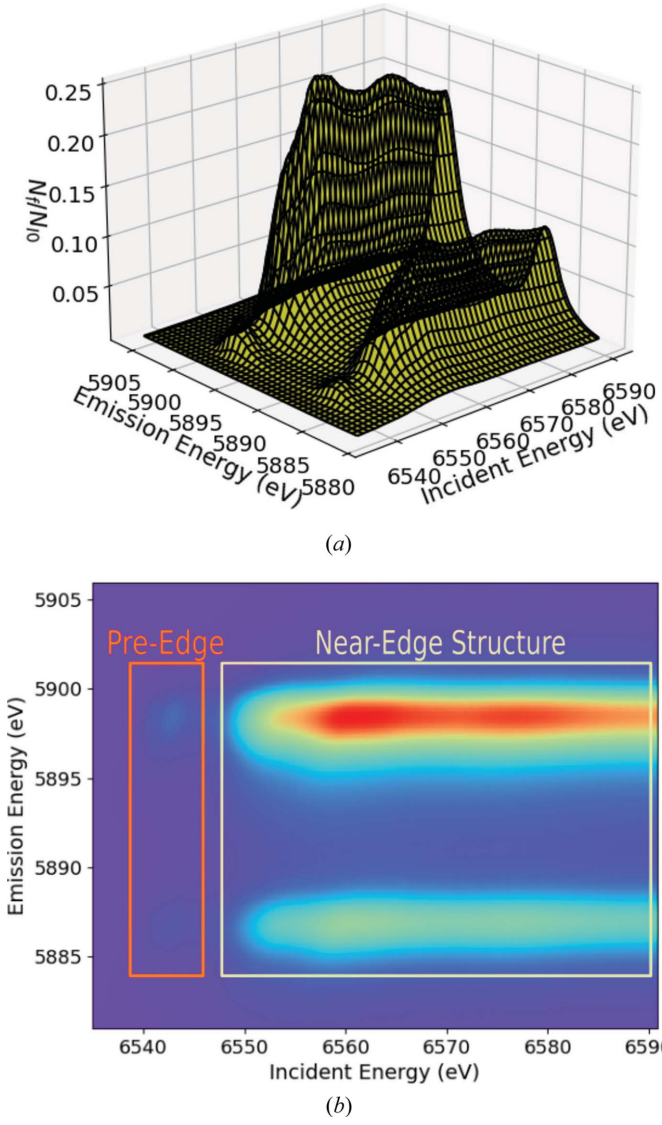

Figure 4
A RIXS map of MnO_2, presented as both a surface plot (*a*) and a heat map (*b*), showing pre-edge and near-edge structure.

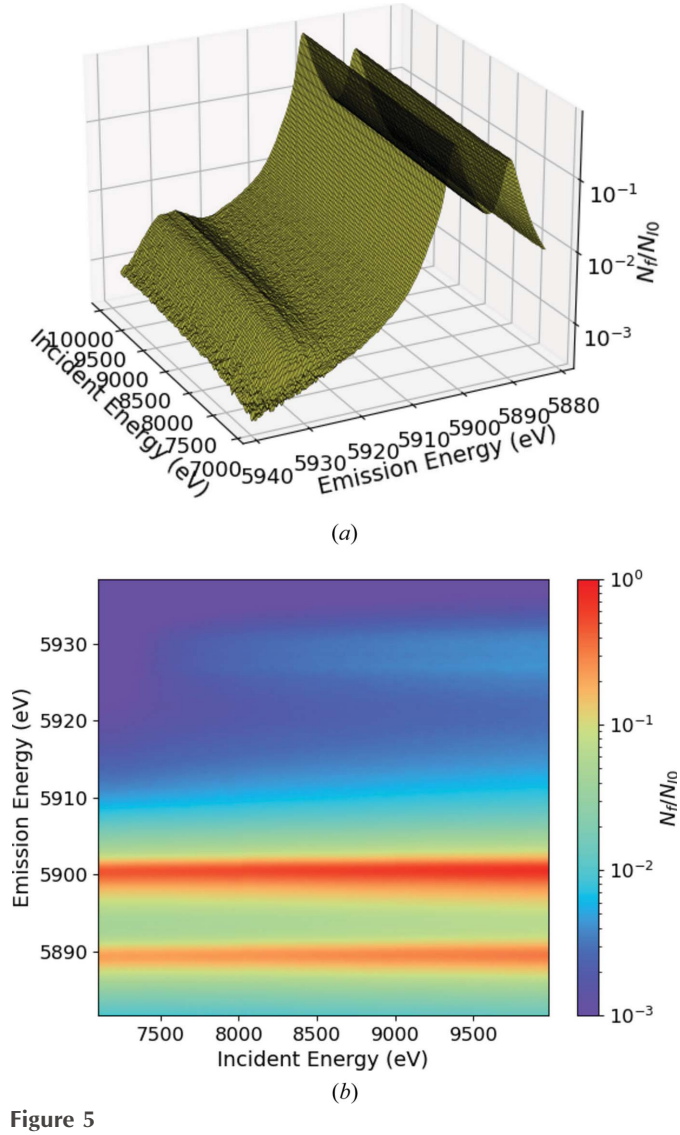

Figure 5
An XR-HERFD scan of Mn $K\alpha$, presented as both a surface plot (*a*) and a heat map (*b*), showing the presence and evolution of the $K\alpha_{3,4}$ transition.

and fluorescent energy axes are measured by holding the analyser crystals fixed and scanning over the incident energy axes, and then moving the crystals to the next emission energy to repeat the process. However, the scans are over very different ranges of energy, with incident energy ranges in particular extending for several kiloelectronvolts, targeting novel and unknown processes, and they are not focused on resonant transitions as the incident energy ranges are typically above the pre-edge and edge regions.

2.5. Data presented for this study and discussion

The primary data for this paper and analysis are the XR-HERFD scans from three experimental runs at Diamond. Of the experiments conducted, Experiments 2 and 3 differed from Experiment 1 through a higher cutoff in the harmonic rejection mirror, resulting in higher flux at higher incident energies as discussed further in Section 4.4. Critical contributing data include sets of elastic scans to investigate energy calibration, offsets and resolution, and pre-processing and analysis. Illustrations are also presented from other selected data scans and scan types collected during those experiments.

3. Data forms, preprocessing and analysis

3.1. Binary and ASCII forms

There are two different data outputs returned from the detectors and software. The first is a simple ASCII text file that contains eight columns giving the incident energy, the fluorescent energy, the Bragg angle, the incident intensity, the total counts recorded on the MAXIPIX detector within a predetermined region of interest (ROI), the ratio of the total counts to the incident intensity, the time over which the measurements were taken and the maximum value of the MAXIPIX detector within the defined ROI.

The second form, NeXus (Könnecke *et al.*, 2015) HDF5 binary files, contains the value of each pixel in the MAXIPIX detector for each individual measurement. The benefit of this data format is that it enables a far deeper investigation into the data by isolating specific regions. The NeXus format conveys data organized according to the character state data model. Hierarchical Data Format (HDF) is a set of file formats (HDF4, HDF5) designed to store and organize large amounts of data. This format can be initially processed with the *Data Analysis Workbench* (*DAWN*) software package, developed in house at the Diamond Light Source (Filik *et al.*, 2017), or by purpose-driven pre-processing software.

3.2. Limitations of ASCII from RIXS and HERFD, or the need to analyse binary data files

The ASCII text file output for each spectrum is generated by integrating over all the pixels in a predefined region on the MAXIPIX detector at each energy. This yields a much smaller and easy-to-process format, perhaps for normal XANES or XAFS analysis, but leads to a loss of energy resolution and spectral structure, with additional systematics included such as mismatched energy calibration and poor background subtraction, as discussed below.

3.3. Past approaches

Regular fluorescent XAFS experiments performed by integrating over a large or medium range of fluorescent energies are typically analysed by comparison with self-consistent *ab initio* calculations of the fine structure usually performed with the *FEFF* (Ankudinov *et al.*, 2002) software package or other density functional theory calculations (Joly *et al.*, 2009) to confirm solid-state properties such as nanostructure. The 2D RIXS spectrum of Mn has been reported (Glatzel *et al.*, 2004) using elastic scans to help define the emission energies and resolution, though like most RIXS experiments this one focused on the resonant, *i.e.* bound–bound, pre-edge structure. HERFD-XAS measurements, *e.g.* by Safonova *et al.* (2006) and Glatzel & Bergmann (2005), are typically performed and analysed in a similar manner to regular XAS experiments but using the higher resolution of HERFD scans. Here, we separate the multiple crystal images on the detector in a similar manner to Hayashi *et al.* (2004) and Moretti Sala *et al.* (2018), and are thereby able to isolate systematics, improve energy calibration and improve resolution.

3.4. Quantifying the intrinsic alignment and efficiency of analyser crystals

Examining the binary output files of each analyser crystal individually allows identification of issues and inconsistencies in the data. The left analyser crystal in Experiment 1 exhibited some 20% less intensity than the other two crystals (Fig. 6), so that the statistics and consistency were not uniform, and it also exhibited discontinuous spectra (Figs. 7 and 8). This issue was tracked down to a mechanical fault in one of the motors, which failed to reach the correct position for the next Bragg angle

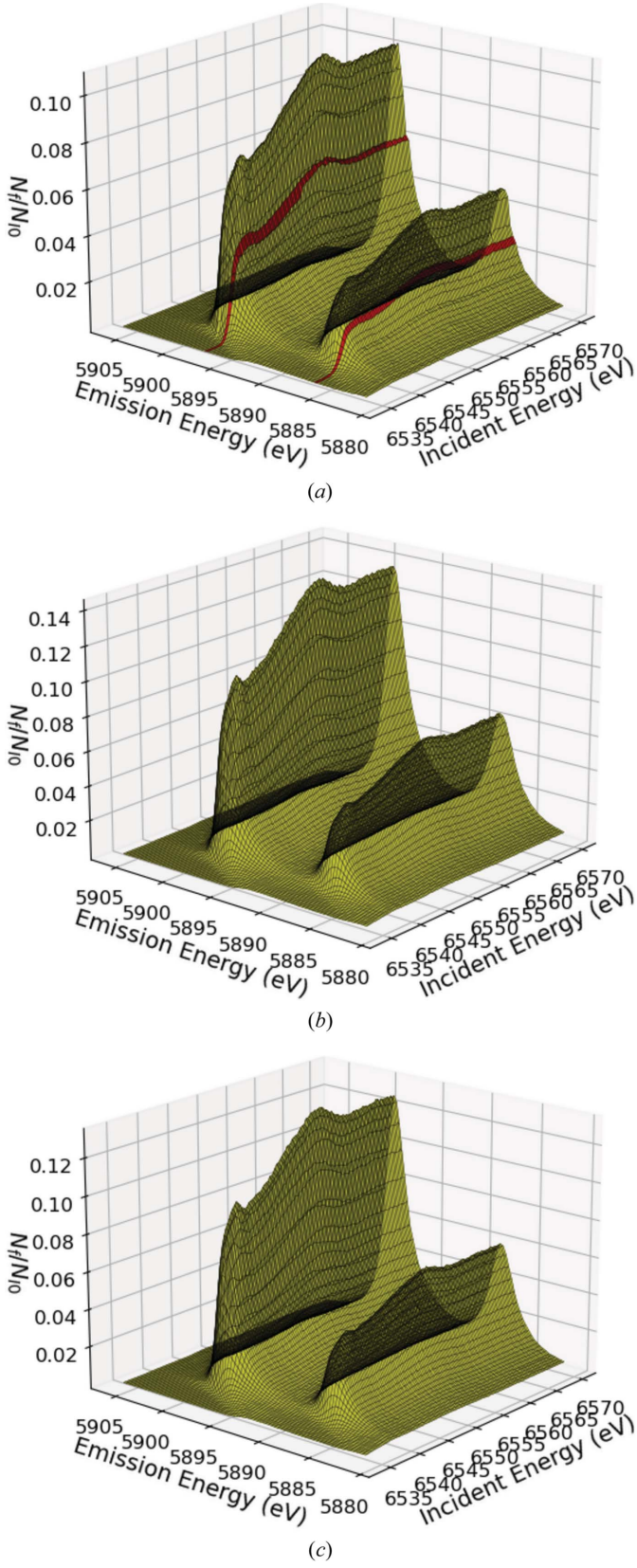

Figure 6
RIXS maps of normalized intensity N_F/N_{I_0} taken from (*a*) the left, (*b*) the centre and (*c*) the right of the three analyser crystals. The left crystal image has significantly lower intensity (20%) and is noticeably noisier (consistent discontinuities in the stepper motors are illustrated in red), as also shown in Fig. 7(*a*).

when performing an XES scan (Fig. 7). It was later resolved by fitting a new spring, allowing Experiments 2 and 3 to include all three analysers.. By isolating the faulty region in the binary data, we could exclude these measurements from the data, which removed this systematic effect. This analysis and resolution would have been impossible if only the total raw output was used. These experiments only used three analyser crystals. The beamline has since been upgraded to 14 analyser crystals. Other beamlines and facilities such as ID20 at the European Synchrotron Radiation Facility (ESRF, Grenoble, France) have up to 72 analyser crystals. The ability to isolate

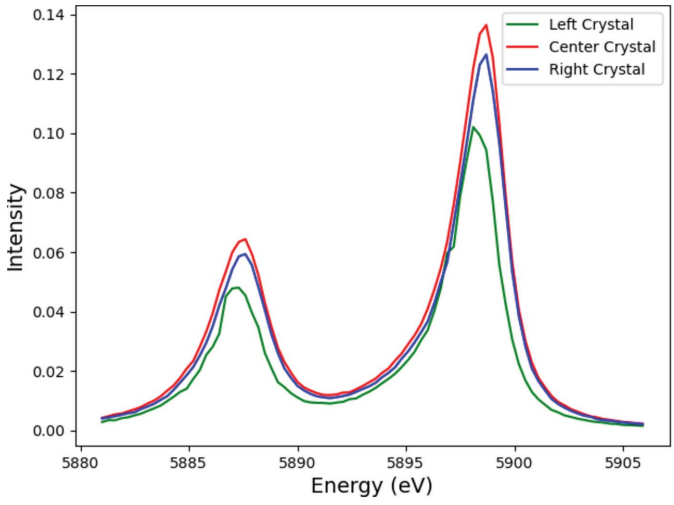

(*a*)

(*b*)

Figure 7
Detection, diagnosis and correction for experimental and alignment defects. (*a*) XES spectra from each analyser crystal. The left crystal signal exhibits significant noise and inconsistency, with an energy offset, compared with the central and right crystals. (*b*) A RIXS map using the left analyser crystal, showing a major discontinuity (harmonic) at 5896.9 eV in the fluorescence spectra for all incident energies, due to a faulty motor. For this reason we discarded the left crystal from further analysis of Experiment 1. Without the separation of the crystals, diagnosing this systematic would have been far more difficult and the data from the other crystals would have been compromised. In Experiments 2 and 3, this issue was rectified and could also be proven from the data analysis and separation.

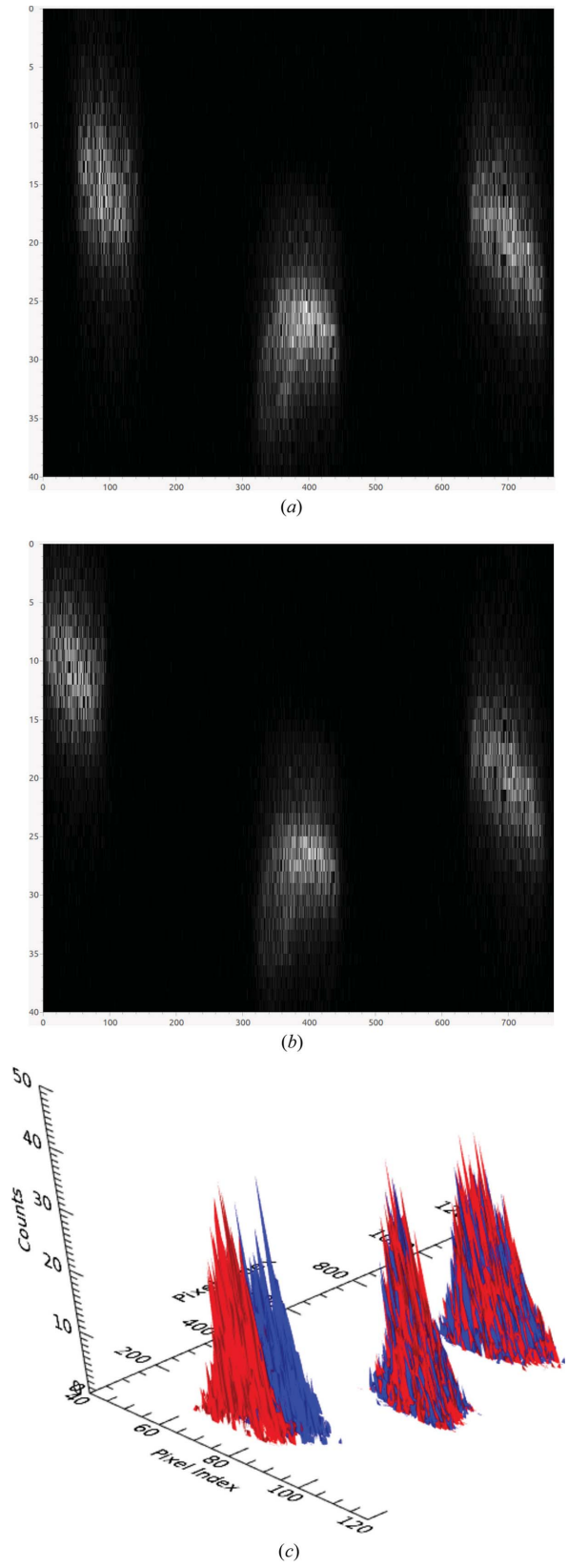

(*a*)

(*b*)

(*c*)

Figure 8
(*a*) and (*b*) Maps of the pixel detector during measurements of Mn foil with fluorescence energies of (*a*) 5886.1 eV and (*b*) 5886.4 eV, showing a vertical shifting of the left ROI. (*c*) A surface plot of the above two index plots overlaid on top of one another; blue = 5886.1 eV and red = 5886.4 eV.

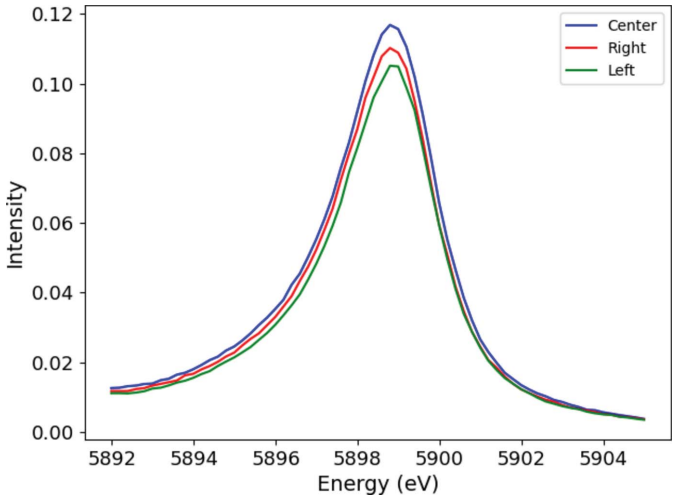

Figure 9
In comparison with Experiment 1 [Fig. 7(*a*)], the motor alignments are all optimized, and they are fixed in Experiments 2 and 3.

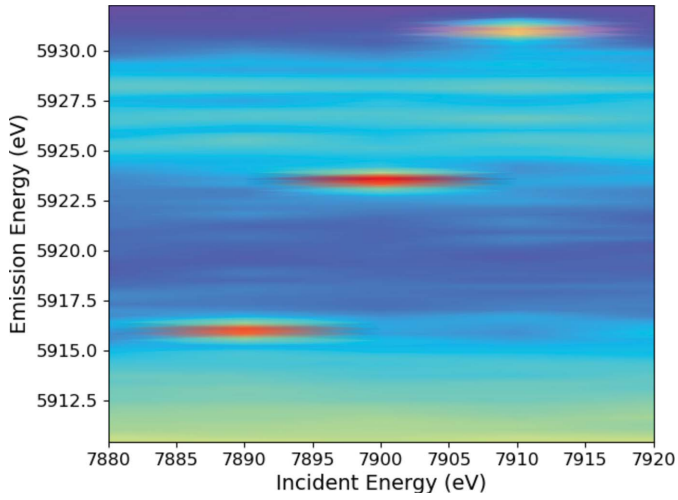

Figure 10
Anomalous peaks can be seen in the data at (E_i, E_f) = (7890, 5915.9), (7900, 5923.5) and (7910, 5931.1) eV. The cause of these was not immediately obvious but they certainly affect the structure and signature of an important area of the spectrum. As discussed in the text, these are due to diffraction of elastically scattered photons by the analyser crystals.

measurements from any defects, like that described above, which might arise in any one of these several highly sensitive analysers over the course of a scan that may take hours is another significant benefit of this technique.

This separation of images and binary investigation can provide quality control over the crystal alignment, diffraction angles and mechanical motor stability. Fig. 8 indicates that the three crystals are not aligned at the same height so may correspond to different Bragg angles and hence energies, which will lower the resolution and spectral structure. Further, the peaks of the images are found at vertical pixels 15, 28 and 20 for the three images. Due to the motor problem, the peaks at the next energy are found at pixels 10, 28 and 20, a non-uniform change of energy in the spectra. The 18-pixel offset could correspond to a 1.5 eV shift in energy between crystals. This mismatch in calibration can be attributed to the yaw component of the analyser crystals required to separate the crystal regions on the detector effectively, especially in Experiment 1. This was fixed, with good consistency achieved for later measurements as shown in Fig. 9.

3.5. Diffraction of elastic peak by analyser crystals

When looking at regions of our data where the intensity is very low, we can occasionally observe a series of anomalous intensity spikes in the data (Fig. 10). These anomalies are observed in all three crystal regions and occur at regular intervals. Furthermore, no abnormalities in the MAXIPIX detectors are observed, with crystal regions remaining stationary and no additional features appearing. Integrated counts are normalized by the incident photon intensity.

The analyser crystals filter out unwanted scattered photons outside the narrow Bragg peak; however, when certain conditions are met (elastically) scattered photons can satisfy the Bragg equation for different diffraction planes (Fig. 11). The germanium analyser crystals in these experiments are tuned to the (333) plane. Hence, elastically scattered photons from the sample can also satisfy the Bragg equation for the (444) plane for incident energies that correspond to

$$\lambda = 2d\sin(\theta) = \frac{2a_0\sin(\theta)}{(h^2+k^2+l^2)^{1/2}} \Rightarrow \sin(\theta) \propto \frac{(h^2+k^2+l^2)^{1/2}}{E}. \quad (2)$$

If the Bragg angle is the same for both the incident (E_i) and fluorescent (E_f) energies then

$$\frac{E_i}{E_f} = \frac{(h'^2+k'^2+l'^2)^{1/2}}{(h^2+k^2+l^2)^{1/2}} = \frac{(3\times 4^2)^{1/2}}{(3\times 3^2)^{1/2}} \Rightarrow E_f = 0.75\,E_i, \quad (3)$$

where (h', k', l') refer to the Miller indices of the plane the elastically scattered photons are reflecting off. Given that germanium has a diamond lattice, we check the selection rules for allowed reflections of which there are two: for the first, h, k, l are all odd, and for the second, h, k, l are all even and $h + k + l = 4n$. The (444) plane satisfies the second of these and so is allowed. Whenever the incident energy is equal to three quarters of the fluorescent energy selected, these spikes in intensity occur. Once identified, the spikes can be removed and replaced with the average measurement of the four adjacent pixel measurements in the incident energy direction. We observe the same phenomenon at higher energies (Fig. 12), corresponding to elastically scattered photons diffracting from the (555) plane,

$$\frac{E_i}{E_f} = \frac{(3\times 5^2)^{1/2}}{(3\times 3^2)^{1/2}} \Rightarrow E_f = 0.6\,E_i. \quad (4)$$

These elastic peaks appear as isolated peaks in Figs. 10 and 12 due to our large incident energy step size relative to the fluorescent energy step size (30 and 0.3 eV, respectively). As a result, all of the adjacent pixels in Figs. 12 and 11 will be free of this systematic, giving the appearance of isolated peaks. A

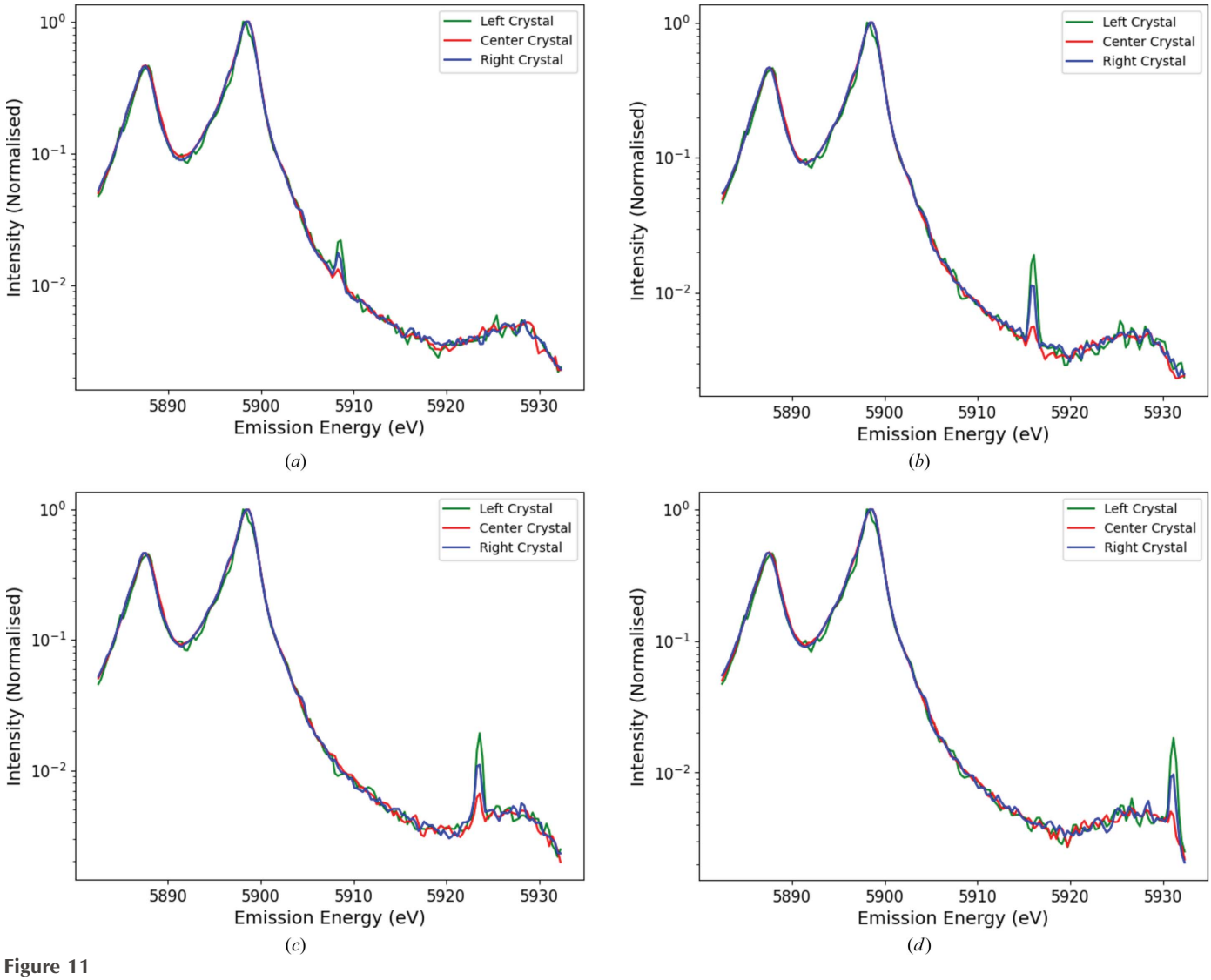

Figure 11
Mn $K\alpha$ spectra at incident energies E_i of (*a*) 7880, (*b*) 7890, (*c*) 7900 and (*d*) 7910 eV. The elastic diffraction peak can be observed for each of the three analyser crystals.

much smaller incident energy step size would reveal a continuous elastic diffraction line.

The intensity of the 444 reflections of elastic scatter from the central analyser crystal is noticeably lower than that in the left and right analysers (Fig. 11). Since the elastically scattered photons mainly arise from Rayleigh scattering, the intensity is 0 at 90° to the initial beam direction. As the central crystal is aligned at 90° to the beam, the effect is minimized for this region.

A final note is that the positions of the harmonics shown in Figs. 10 and 11 of (E_i, E_f) = (7880, 5908.5), (7890, 5915.9), (7900, 5923.5) and (7910, 5931.1) do not match exactly with the equivalent values predicted by equation (3) of (E_i, E_f) = (7880, 5910.0), (7890, 5917.5), (7900, 5925.0) and (7910, 5933.5). The emission energy values of the harmonics all appear to be ∼1.5 eV lower than predicted. These measurements were taken from our first XR-HERFD experiment and, as we discuss later in Section 4.4, there was a slight offset in the

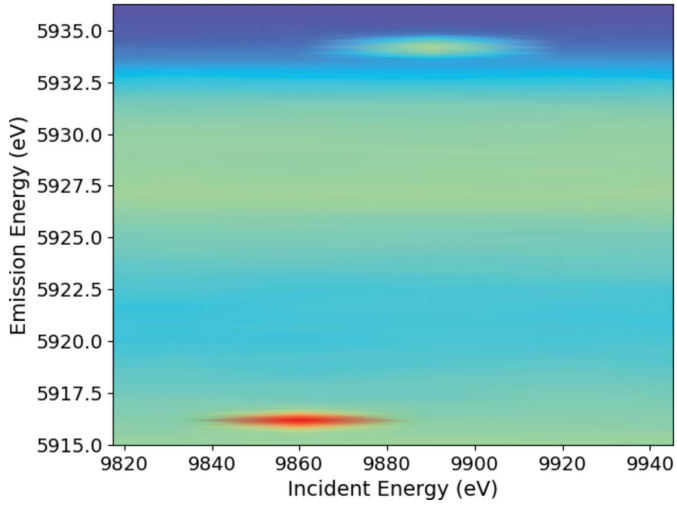

Figure 12
Elastic scattering and diffraction from (555) is also observed at (E_i, E_f) = (9860, 5916.2) and (9890, 5934.2) eV.

emission energy calibration of −1.6 eV which explains this observed discrepancy in the harmonic positions.

4. Dramatic resolution improvement using binary data splicing

Chantler (1992) and Chantler & Deslattes (1995) discuss Johann geometry broadening arising from the intrinsic ideal Bragg spectrum combined with the depth penetration of the incident photons and the strain of the crystal, causing both geometric and energy broadening of the resultant focal point on the Rowland circle and detector (Kowalska *et al.*, 2016). There have been several techniques developed over the years to attempt to improve the performance of analyser crystals (Masciovecchio *et al.*, 1996; Huotari *et al.*, 2005; Kavčič *et al.*, 2012). Due to the excellent spatial resolution of our data delivered by the MAXIPIX detector, it is possible to refine the energy resolution of the measurements by partially removing the broadening intrinsic to the Johann geometry analyser crystals in a similar manner to Honkanen *et al.* (2014).

The elastic scans give an ideal definition of the limiting resolution function of the detector: given explicitly, the beam divergence and convergence; the beam bandwidth; the beam slit size on the sample; the beam harmonic contamination at the sample; the sample thickness, roughness, composition and angle to the beam; the sample angle to the detector analyser crystals; and in effect, the whole beamline X-ray optics. Hence, if the bandwidth were a Dirac δ function and the sample scattering were also a Dirac δ function, then the crystal diffraction would map out the XES spectrum for the characteristic radiation and, for a particular setting, would provide something close to the intrinsic Bragg width, subject to imperfections in the analyser crystal structure and curvature. By choosing an elastic scan, especially from the side of the sample mount, well below any RIXS structure or the pre-edge, the spectrum diffracted is almost purely the elastic scattered radiation from the sample.

Hence, imperfections can be seen in the non-uniform curvature and offsets of the detector image. Therefore, a spectrum is isolated from each narrow horizontal stripe defined as in Fig. 13, and a shift of the centroid in energy away from the correct centre of the spectrum (defined by fitting a Gaussian to the spectrum obtained when taking the sum of the entire crystal region) is observed. This was also investigated in the horizontal direction. Unsurprisingly, we find that the dominant effects are in the dispersion direction (*i.e.* vertically). Whereas this beamline was hitherto considered to have an intrinsic limiting resolution or point spread function of approximately 1 eV, the raw integrated elastic scan images give a FWHM of 0.78 eV in this case (at this incident energy and Bragg angle, with this analyser crystal and alignment) and the splicing correction shows that the limiting resolution of the optic of the beamline under these normal conditions is 0.36 eV.

This methodology may be used to investigate any intrinsic resolution and any change in intrinsic resolution from any change in the optics, beam size, beam divergence, beam bandwidth, sample thickness, sample concentration, sample angle and other relevant parameters. Clearly, a dramatic improvement in resolution is possible with this same beamline and optics. Performing this methodology on our data significantly improves the resolution (Fig. 14), where the FWHM of the corrected spectrum decreases by 54% in our case from 0.78 to 0.36 eV on the XES axis (the emission energy axis). The resolution of a given peak depends upon the intrinsic width of the peak, together with the resolution of the beamline, which is a function of the optics, monochromation, spot size and focus on the sample, thickness of the sample, type of crystal analyser, and spectrometer angle. The resolution and broadening are also energy dependent. It is clear that this will be best observed and calibrated by an elastic peak, with a possible almost-Dirac δ function in energy if the beamline is well monochromated. In the XAS axis, any increase in resolution is hard to see and obscured by the natural (hole) width and structure of the characteristic radiation spectra. Ergo, this

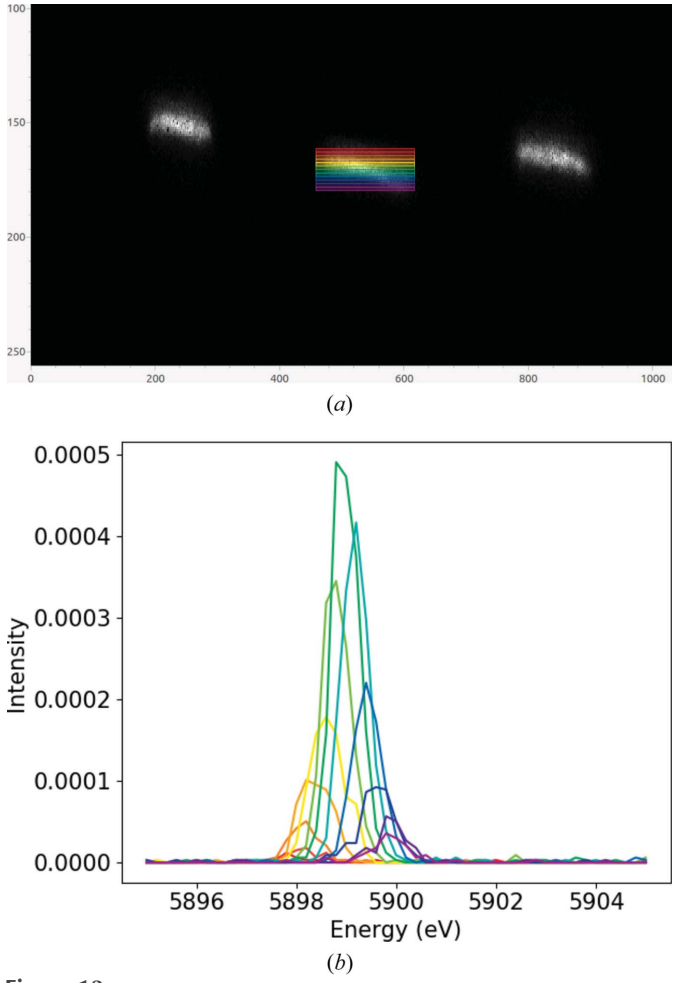

Figure 13
(*a*) Output from the MAXIPIX detector for an elastic scan of the beam where the three crystal regions can be seen. Overlaid on the central crystal region are a series of stripes (each three pixels high). (*b*) The resultant spectra extracted from each stripe. Moving down the vertical plane of the central crystal region, the extracted spectra shift in energy, meaning that unwanted broadening will be introduced when the sum of all spectra is taken, as it traditionally would be. Stripe colours in panel (*a*) correspond to line colours in panel (*b*).

can assess and optimize the limiting point spread function of any advanced HERFD-XAS, HERFD-XAS, RIXS or XR-HERFD arrangement. The HERFD-XES or HERFD-XAS spectrum is likely to be much broader than this. Any such broadening will then be due to the physical and chemical materials structure, which can be interrogated by advanced theory, rather than just being neglected as intrinsic instrumental broadening. For example, measurements of the Mn $K\alpha$ spectrum will be fundamentally limited by the lifetime broadening of the $2p_{\frac{1}{2},\frac{3}{2}}$ hole (0.97 and 0.36 eV, respectively) (Campbell & Papp, 2001; Chantler & Bourke, 2024).

The elastic scan is defined on the XES axis and the improvement is directly observable. Perhaps surprisingly, but certainly significantly, applying this same correction to the 2D spectrum improves our measurement resolution and consistency in the XES axis and yields significant improvements in the XAS absorption spectrum without any additional analysis.

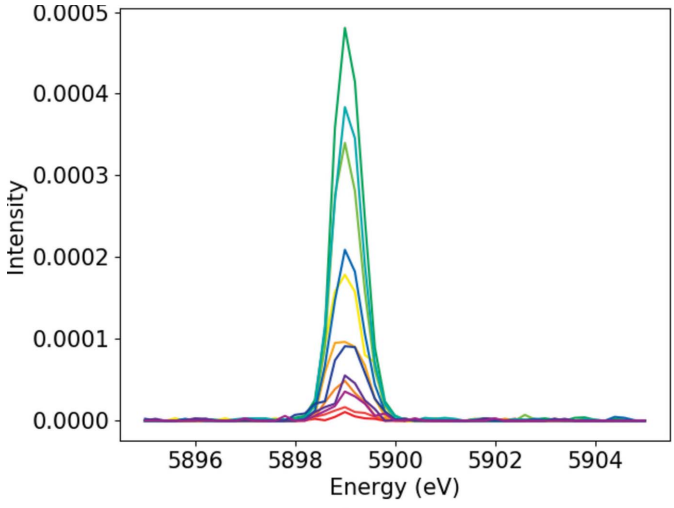

Figure 14
(*a*) All the spectra from Fig. 13(*b*), after they have been shifted to a consistent reference position. (*b*) The sum of all of the shifted spectra (blue) compared with the lower-resolution original integral (red).

Despite no explicit correction being applied to the XAS axis, we see significantly better consistency for the spectra across the absorption edge after the XES spectra have been shifted (Fig. 15). Note that the shifts in energy and edge on the scans taken from the upper region of the crystal ROI on the detector are of a lower intensity than those for the central region, and these shifts partially cancel out the shifts of the lower pixels. There should not be any net shift in energy, as observed. Further, the increase in resolution in this XAS axis is hard to observe and quantify for the reasons given above, but it is clear that part of the broadening is indeed suppressed. The resolution of the edge region in the HERFD-XANES scan is nonetheless improved, and quantification suggests an improvement in resolution of an electronvolt or more, complicated by the width and structure of the edge. The

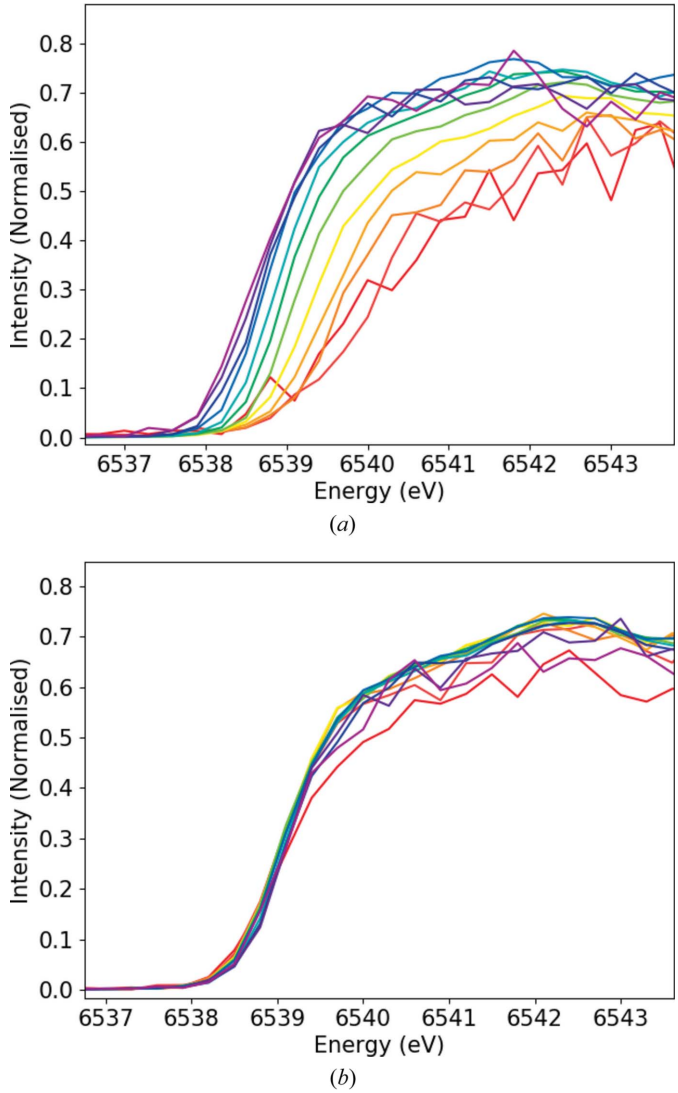

Figure 15
Comparisons of the XANES spectra of Mn obtained from each of the stripes defined in Fig. 13(*b*), (*a*) before and (*b*) after the XES spectra have been spliced and realigned as per the elastic scan analysis, which can equally be applied to any spectrum or scan modality. No correction has been applied to the XAS axis, yet we see dramatically better agreement of the spectra, and improved resolution for any near-edge structure, across the absorption edge.

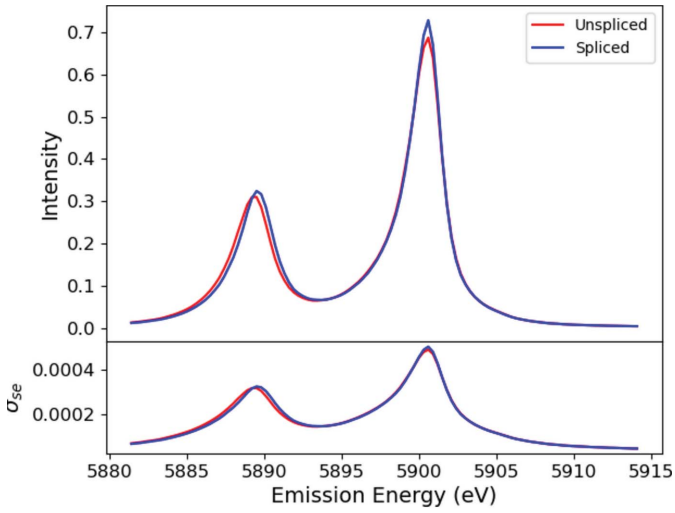

(*a*)

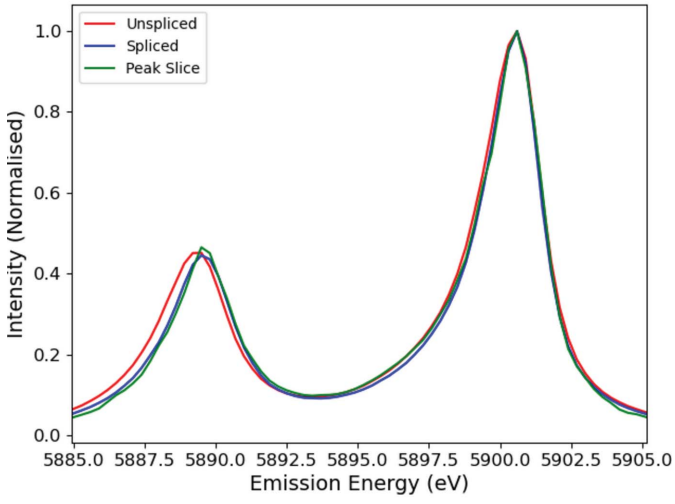

(*b*)

Figure 16
(*a*, upper plot) The emission spectrum of Mn (as shown in Fig. 15) both before (red) and after (blue) splicing processing, demonstrating increased intensity, higher resolution and a slight peak shift in $K\alpha_2$ (depending upon the processing reference). (*a*, lower plot) Standard error uncertainties (σ_{se}) are presented here for the first time and are essentially unaffected by the splicing processing. (*b*) The same data as in panel (*a*) but including the spectrum from a single horizontal slice through the peak of the crystal region, with all three spectra normalized. The single spectrum should be free from the majority of broadening effects in the raw spectrum but has much lower intensity and worse statistics than the others (and is thus noisier).

improvements to the Mn $K\alpha$ spectrum by applying this technique are illustrated in Fig. 16, where we see that a slight shift in the $K\alpha_2$ peak is observed. Comparing the spliced and unspliced spectra with a spectrum taken from a single horizontal slice through the peak of the crystal region, we see that the peaks align much better with the spliced spectrum. This implies that the slight energy shift observed in $K\alpha_2$ is real.

4.1. Correction for background scatter

A rarely considered source of systematic error in pixel detectors is that of background noise. The MAXIPIX detector returns non-zero values in regions away from the locations of the analyser crystal images, where there are no X-rays from diffraction. This background can be caused by electronic noise or stray gamma and cosmic rays, but is dominated by fluorescent photons coming straight from the sample to the detector. Given that these photons make up the full emission spectrum, they do not correspond to the specific energy selected with the analyser crystals. These background counts are observable in the binary images and can be corrected for in the pre-processing of the spectrum. By taking an average over a wide range of pixels in the MAXIPIX detector where there are 'no' X-ray peaks, we obtain a value of the average number of background counts per pixel which can then be subtracted from the regions containing data. The error in the number of background counts per pixel is determined by taking the standard error of the spread in the background counts at each energy. This background region is selected to ensure that it is isolated from any crystal image and that the counts are random, verified by taking the weighted average of the centre of mass of the background counts at each incident and emission energy combination and ensuring that it is always within two standard deviations (defined as the standard error of the spread in the background counts across the region) of the weighted average of the centre of the defined region.

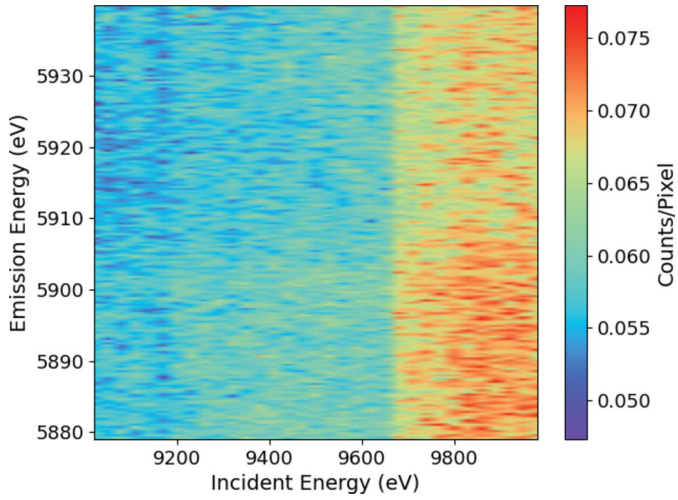

Figure 17
Background counts per pixel where a clear and spontaneous increase is observed after 9660 eV, apparently due to a small signal from zinc contamination reaching the detector.

Performing this analysis reveals an energy dependence for the background counts. Once the incident energy increases above ~9660 eV, the magnitude of the background spontaneously increases by roughly 24% (Fig. 17). An energy of 9660 eV corresponds to the K absorption edge of zinc, suggesting that there was some small zinc contamination in our experimental optics which reached the detector. By making use of the 2D nature of the detector, and characterizing the background in this way, the effect of this contaminant can easily be removed from the measurements with the introduction of negligible error (Fig. 18). Any other contaminants contributing unwanted counts to our measure-

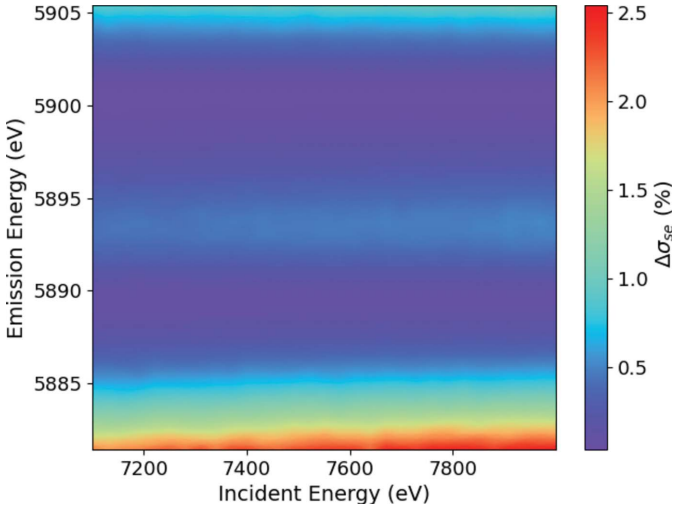

Figure 18
The percentage increase in σ_{se}, $\Delta\sigma_{se}$ (%), due to the inclusion of error in background counts.

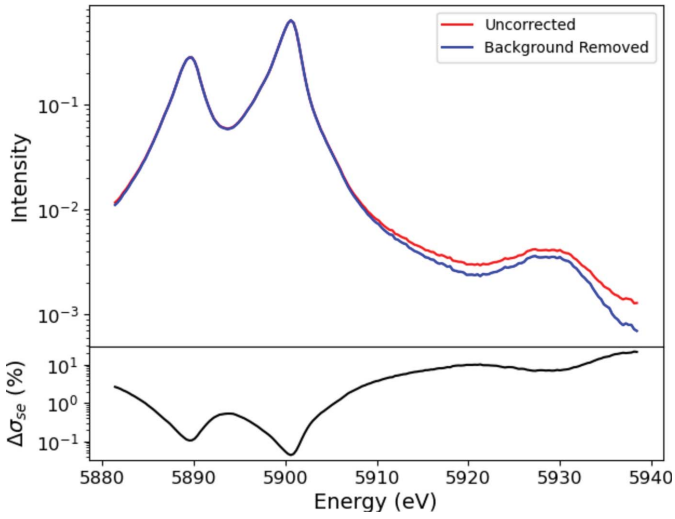

Figure 19
The emission spectrum of Mn with (blue) and without (red) the background counts subtracted. The effect of the correction is significant in the low-intensity tails where the intensity is reduced by 23%. The percentage increase in σ_{se}, $\Delta\sigma_{se}$ (%), due to the inclusion of error in background counts is shown.

ments would be likewise eliminated from the data set. The effect of this background subtraction is illustrated in Fig. 19; in the low-intensity tails, the intensity is reduced by 23%, making this a significant correction to apply when looking at low-intensity transitions.

4.2. Determination of uncertainty

Due to the large amount of time that is required to perform a full RIXS or XR-HERFD scan, repeated measurements are often not feasible. Hence the estimation of uncertainty follows best from adjacent point-wise estimation of noise, from reproduced overlaid quantification of noise from different crystal analysers, and from the notional normally distributed counting statistic for upstream monitor signals and the dominant detector image counting signals. Hence the number of counts N returned by each pixel represents the mean of a binomial distribution with standard deviation $N^{1/2}$. This can also be thought of as treating the counts with Poisson statistics. When integrating the pixel counts, the total counts have a standard deviation of

$$\begin{aligned}\sigma_{F_i} &= \left(\sigma_1^2 + \sigma_2^2 + \cdots + \sigma_n^2\right)^{1/2} \\ &= (N_1 + N_2 + \cdots + N_n)^{1/2} = \left(N_{F_i}\right)^{1/2},\end{aligned} \tag{5}$$

where n is the total number of pixels and F_i is the ith crystal image on the detector. The ratio of the number of fluorescent photons N_{F_i} reaching the detector from one crystal analyser to the number of incident photons N_{I_0} in the upstream ion chamber, N_{F_i}/I_0, is the quantity of interest, with the statistic normally dominated by the number of counts on the detector image.

Similarly, the background signal $N_{\rm bg}$ is measured over a range of pixels well away from the crystal images for $n_{\rm bg}$ pixels, each having uncertainty $\sigma_{\rm sd,bg}$ (where $\sigma_{\rm sd}$ is the standard deviation), so that the background signal for each crystal image region is $N_{F_{i,\rm bg}} = N_{\rm bg} n_{F_i}/n_{\rm bg}$. Then with $N_{F_{i,\rm net}} = N_{F_i} - N_{F_{i,\rm bg}}$, $\sigma^2_{F_{i,\rm net}} = \sigma^2_{F_i} + \sigma^2_{F_{i,\rm bg}}$.

The equations for the weighted standard deviation depend upon whether the individual data sets are consistent or inconsistent, especially with respect to each crystal analyser ROI. For example, each crystal has a different efficiency and a different self-absorption from the angle from the sample surface. Therefore, these numbers would be inconsistent unless scaled. They are scaled to the peak channel in energy of the spectrum, so that the remaining variance is ideally due to consistent noise. The weights are

$$w_i = \frac{1}{\sigma_{F_{i,\rm net}}} = \frac{1}{\left(N_{F_i} + N_{F_{i,\rm bg}}\right)^{1/2}}. \tag{6}$$

Then the weighted average per crystal analyser, $\overline{N_{F,w}}$, is

$$\overline{N_{F,w}} = \frac{\sum_i a_i N_{F_{i,\rm net}} w_i^2}{\sum_i w_i^2}, \tag{7}$$

where a_i is the efficiency and self-absorption scaling for a given crystal, and $a_i = 1$ for the strongest (central) crystal. The others are typically about 1/0.8. When the data sets and σ_{F_i} are consistent, then the weighted standard deviation (abbreviated sd) for a crystal is

$$\sigma_{{\rm sd},w} = \frac{1}{\left(\sum_i w_i^2\right)^{1/2}}. \tag{8}$$

However, if the individual measurements are inconsistent, as may be the case with the unscaled right and left analysers, then we should use

$$\sigma_{{\rm sd},w} = \left[\frac{\sum_i \left(a_i N_{F_{i,\rm net}} - \overline{N_{F,w}}\right)^2 w_i^2}{\sum_i w_i^2}\right]^{1/2}. \tag{9}$$

Consistency can be examined by assuming that the inconsistent weighted standard deviation is true and looking at the $(a_i N_{F_i} - \overline{N_{F,w}})$ numerator term in equation (9). If the counts are consistent, then the term will tend towards 0, resulting in $\sigma_{\mathrm{sd},w} \rightarrow 0$. If inconsistent, then $\sigma_{\mathrm{sd},w}$ can get quite large. By plotting both estimates, any discrepancies will be revealed and an upper bound for the error may be estimated. Fig. 20 illustrates how the consistent model gives an upper bound on the error, and demonstrates that both the σ_{sd} and the weighted means of each of the crystal analyser signals are indeed consistent. For example, if the data sets are inconsistent, as occurred with the faulty left crystal motor in Experiment 1, then one could continue with the inconsistent standard deviation, but often one might exclude the inconsistent data. With equal weights and counts, the standard error σ_{se} (the error of determining the mean) is

$$\sigma_{\mathrm{se}} = \frac{\sigma_{\mathrm{sd}}}{(n_i)^{1/2}}, \tag{10}$$

where n_i is the number of measurements or, in this case, the number of crystal images, which here was three. This percentage standard error should be equivalent to the population uncertainty just totalling the counts if based on normal distributions,

$$N_F = \sum_i N_{F_{i,\mathrm{net}}}, \quad \sigma_{\mathrm{sd}} = (N_F)^{1/2}, \tag{11}$$

$$\frac{\sigma_{\mathrm{sd}}\{N_F\}}{N_F} = \frac{\sigma_{\mathrm{se}}\{\overline{N_{F,w}}\}}{\overline{N_{F,w}}}. \tag{12}$$

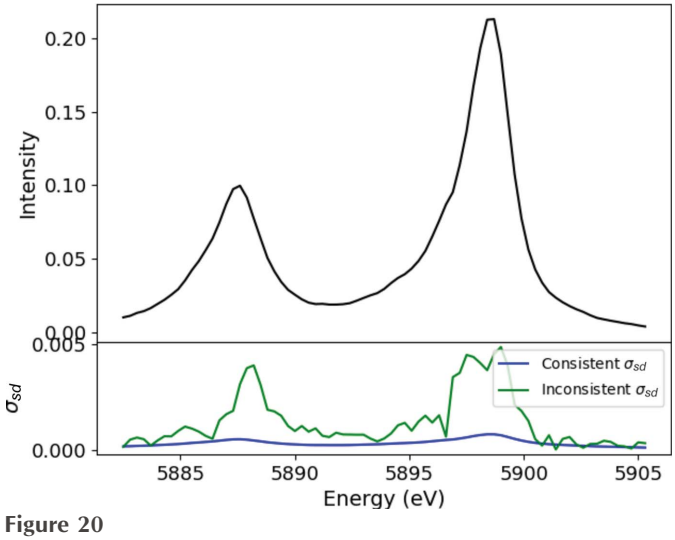

Figure 20
The processed emission spectrum of Mn with estimates of uncertainty based upon the consistent and inconsistent pooling of weighted means. In general they are in very good agreement, with the assumption of inconsistent means leading to a higher uncertainty, especially at the maxima of the derivative where small energy changes in the image regions have a larger impact. These uncertainties are presented for the first time, and it is generally sufficient in this case to use the consistent estimates for further processing and analysis. In the tails, the mean estimates agree very closely where the derivative with energy is small.

Since the upstream ion-chamber counts are measured for each incident and emission energy combination with the three crystal analyser measurements, the weighted mean of the fluorescent counts can be divided by the upstream counts. Given ion-chamber signals are almost never measured in single photon counting mode, and were not in these experiments, the returned count rate N_{I_0} will be given by $N_{I_0} = aN_{\mathrm{counts}}$, where N_{counts} is the true number of single photon counts and a is the amplification decade (Chantler *et al.*, 2000*a*; Chantler *et al.*, 2000*b*). Thus the standard error on these measurements can be given by $\sigma_{\mathrm{se},I_0} = a(N_{\mathrm{counts}})^{1/2} = \left(aN_{I_0}\right)^{1/2}$. Our measurements suggest that the chosen amplification decade has a being approximately 4. Error propagation gives

$$\frac{\sigma_{\mathrm{se}}\{N_F/N_{I_0}\}}{N_F/N_{I_0}} = \left\{\left(\frac{\sigma_{\mathrm{se}}\{N_F\}}{N_F}\right)^2 + \left[\frac{\left(aN_{I_0}\right)^{1/2}}{N_{I_0}}\right]^2\right\}^{1/2}, \tag{13}$$

which is dominated by the fluorescent counts term. Since the upstream measurement as presented is a single point count, there is no correlation relevant between the detector signals and processing.

4.3. Improvement in statistics and resolution

Fig. 16(*a*) illustrates the improvement in resolution for a typical XES spectrum. This is dominated by the detailed structure of the spectrum rather than the experimental and beamline optic broadening, as expected. The improvement is modest but significant. Fig. 20 illustrates application of the two key measures of uncertainty applied to one data set. These estimates are particularly consistent in the spectral tails and are least consistent at the regions of maximum spectral derivative, as expected if there are any energy drifts not accounted for by direct splicing methods. This allows us to have robust estimates of data quality and information content from RIXS,

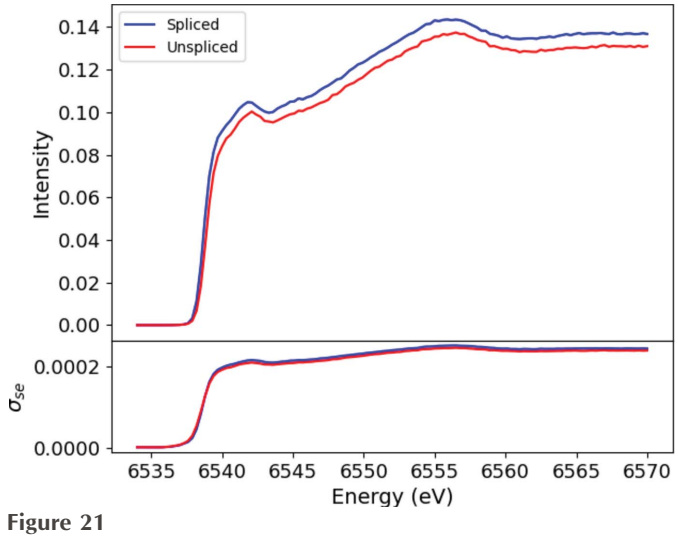

Figure 21
The HERFD-XANES spectrum of Mn along the peak of Mn foil $K\alpha_1$ before (red) and after (blue) splicing, demonstrating increased intensities; the standard error uncertainties before and after are essentially identical but presented here for the first time.

HERFD and XR-HERFD spectra to investigate any physical and chemical process.

Similarly, Fig. 21 illustrates the improvement in resolution for a typical XAS spectrum. The improvement is modest but useful, and confirms the nature of the XAS structure arising from physical processes.

4.4. Energy

This investigation and processing are also significant for defining the edge energy as the point where the gradient of the slope is maximum, since the broadening changes this definition and the location of the edge using standard experimental definitions (as opposed to theoretical definitions). The analysis potentially shifts the position and slope of the edge, and by extension the edge energy, by *e.g.* −0.3 eV from 6539.0 eV to 6538.7 eV. This is important for accurate independent calibration of the incident beam energy, by comparing the measured edge energy with existing standards. The standard reference edge energy of Mn (Kraft *et al.*, 1996) is 6537.67 eV, implying that our incident energy values are discrepant by just 1 eV.

A major challenge and systematic in RIXS and on related beamlines is the calibration or definition of energy in the XAS and XES axes (Glatzel *et al.*, 2021). XES spectra have previously been experimentally calibrated to up to two parts per million (Dean *et al.*, 2019), with the most commonly cited databases generally consisting of the work of Kraft *et al.* (1996), Bearden (1967) and Krause & Oliver (1979). Normally on RIXS-related beamlines these are relative measurements and ideally with constant offsets for different materials. Often the standard XAFS synchrotron approach is used by calibrating the energy of a single absorption *K* edge to the experimental spectrum. Calibration to a single reference edge derivative has problems of bandwidth, beam optics, and the location of the maximum of the first derivative as a function of resolution and pre-edge and white line structure, yet it is also currently used to define the XAS axis energy calibration, at least at a single energy point. It is common to use reference edge energy values from the 'Orange Book' (Thompson *et al.*, 2009) which in turn derives from Bearden & Burr (1967). Other possible sources include Kraft *et al.* (1996), Wong (1999), Deslattes *et al.* (2003) and Chantler *et al.* (2024). We recommend Kraft *et al.* (1996) for the Mn *K* edge, using the first-derivative definition on a good resolution beamline for transmission measurement.

In RIXS-related experiments, the emission energy may then be calibrated to the incident energy via one or more elastic scans. In these experiments, on I20-Scanning, the spectrometer and emission axes are calibrated using the $K\alpha_1$ peak or $K\beta_1$ peak of the emission line. Hence the calibration should be independent of the monochromator (incident beam) calibration and may be about 1 eV different.

The splicing analysis just presented is thus directly relevant as the calibration should follow the resolution improvement. Experiment 1 involved calibrating the absorption edge of manganese to 6539 eV (Thompson *et al.*, 2009) whilst the later

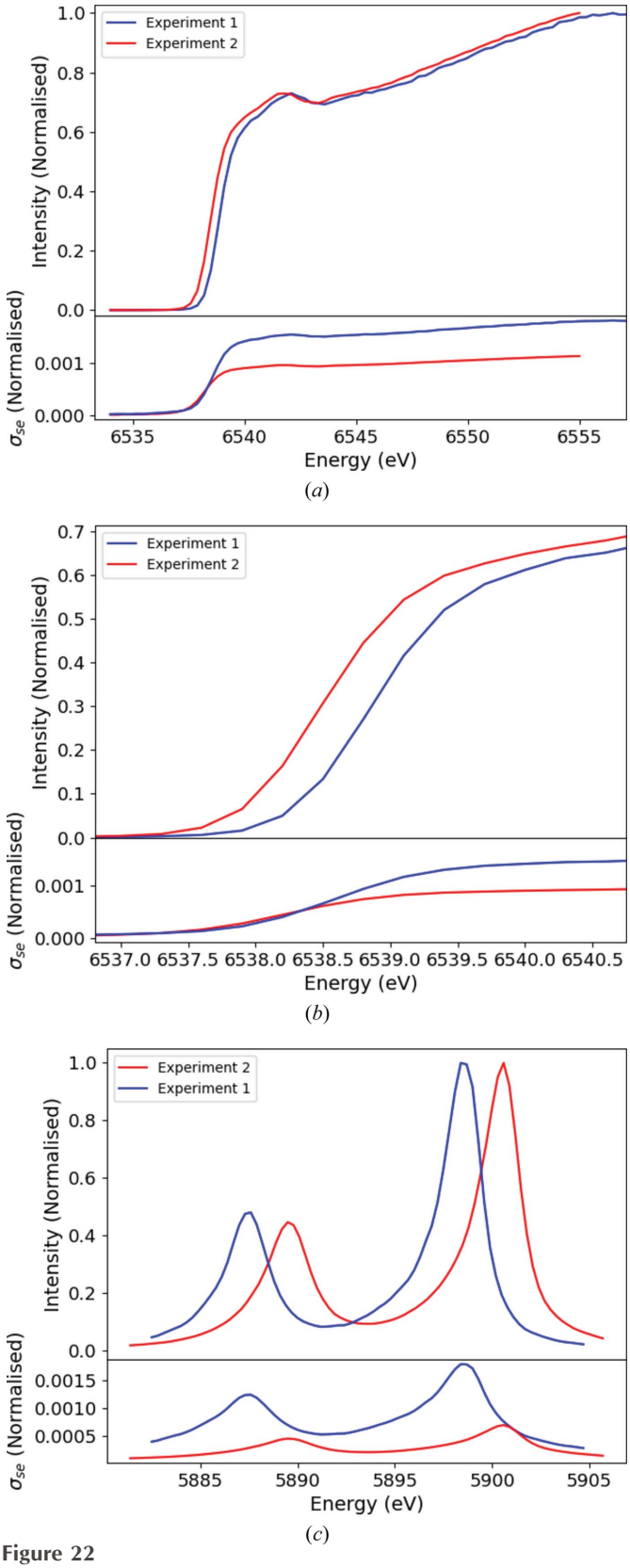

Figure 22
HERFD-XES and HERFD-XANES scans for Experiments 1 and 2. (*a*) The HERFD-XANES axis. (*b*) The HERFD-XANES or XAS axis, expanded. (*c*) The XES axis. Perhaps unexpectedly, the discrepancy between the two in the XES scan is ∼1.6 eV and this is probably due to differences in calibration. In the HERFD-XANES scans we see a difference of ∼ −0.4 eV.

experiments used 6537.67 (Kraft *et al.*, 1996). This means that we should expect to see a discrepancy between our measurements of ∼1.3 eV.

What we see is something interesting and perhaps unexpected (Fig. 22): the incident energy axis energies deviate by approximately −0.4 eV, while in the emission energy axis they differ by 1.6 eV. These offsets depend upon the accuracy with which the edge and then the XES transfer calibration are performed and the statistics and processing of the elastic scattering data. Here we note that researchers certainly must calibrate the spectra against a more robust reference in the future, especially for the investigation of RIXS, chemical shifts, oxidation states and related phenomena. The most accurate energy definitions are always the XES spectral energies, especially at high resolution and in comparison with high-accuracy experimental data. Hence the results in Fig. 22 for Experiment 2 represent the calibrated results.

Finally, we provide comparisons of XR-HERFD spectra for the original (Fig. 23, Experiment 1) and subsequent (Fig. 24, Experiments 2 and 3) experiments with experimental uncertainties, after the above processing and corrections. Note that the counting time per point is the same (1 s per step), I_0 is the same (10^5 to 10^6 counts s^{-1}), and all have an identical setup in terms of ring current (∼300 mA) and wiggler gap (20 mm).

Importantly, Experiments 2 and 3 cover a much larger energy range (7000–10000 eV versus 7000–8000 eV in the XAS spectrum; and 5882.5–5910.0 eV versus 5882.5–5902.5 eV in the XES spectrum) and have much higher statistical accuracy and consistency (0.1–0.4% versus 0.4–1.4% in the same energy range). This is due primarily to the replacement of the harmonic rejection mirror and cutoff, eliminating the significant reduction in incident photons at higher incident energies. The significantly greater range over which the data were collected is particularly due to general improvements in efficiency and optimization of the looping over incident and emission energies.

In Experiment 1 (Fig. 23) (Tran *et al.*, 2023), the harmonic rejection mirror was set to the silicon stripe at 4.0 mrad, yielding a mirror cutoff energy of *ca* 9.5 keV; in Experiments 2 and 3, the harmonic rejection mirror was set to the rhodium stripe at 5.3 mrad (Fig. 24) (Sier *et al.*, 2024) and 5.0 mrad (Fig. 25), respectively, giving a spectral cut off above 12.3 keV or *ca* 14 keV. This yielded significantly higher flux and better statistics at higher energies.

Improvements made to the left analyser crystal, after the inconsistencies in Experiment 1 had been noticed, allowed it to be included in the final intensity measurements of Experiments 2 and 3, thus also significantly improving statistics and reducing error. Most important, though, is the much higher normalized intensity (0.75 versus 0.225 for the $K\alpha_1$ peak channel). For any detailed science, this permits much more insightful investigation of many-body processes and experimental spectra.

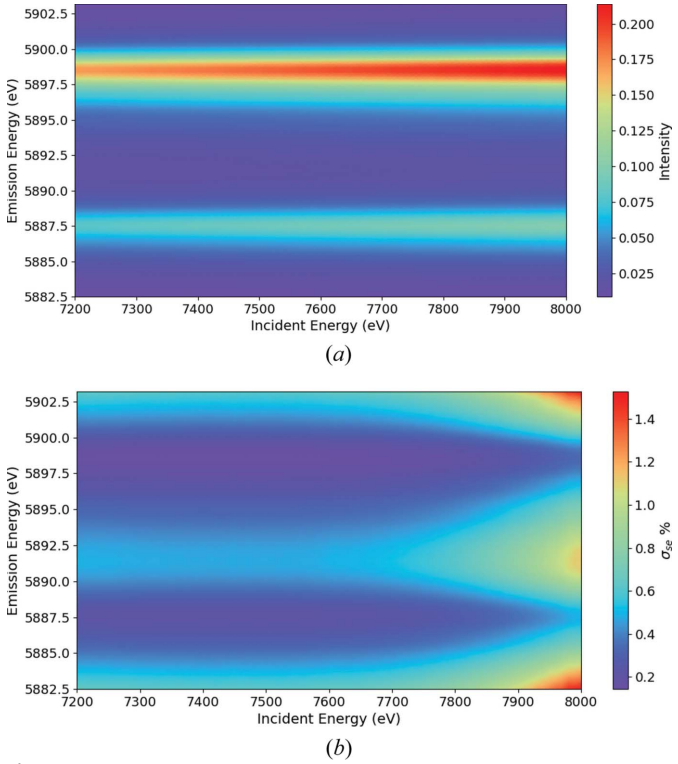

Figure 23
(*a*) An XR-HERFD map of the $K\alpha$ spectrum of manganese taken from Experiment 1. (*b*) The percentage σ_{se} map, showing the quality of the data. The higher uncertainty at higher incident energy results from a reduction in the incident photon intensity due to the cutoff in the harmonic rejection mirror (see discussion of Fig. 25). This is rectified in Fig. 24.

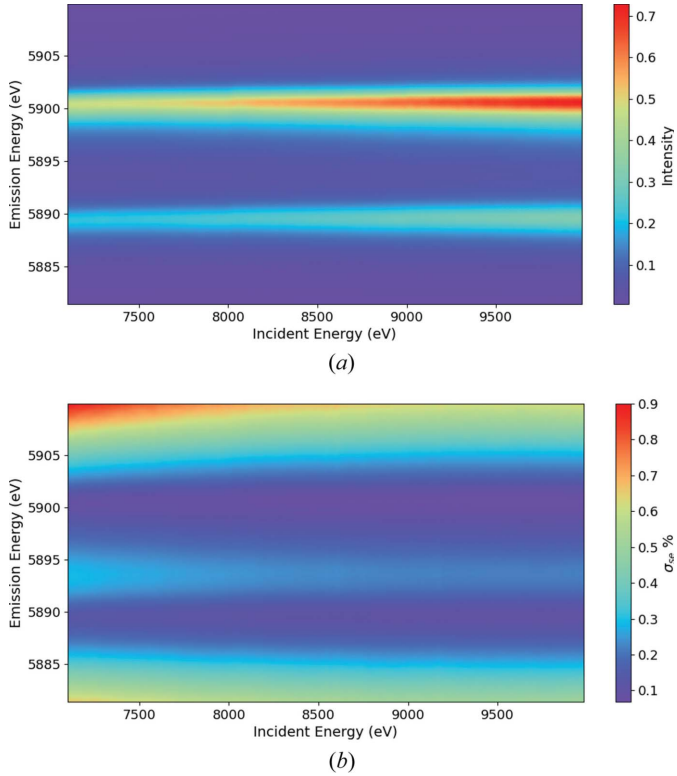

Figure 24
(*a*) An XR-HERFD map of the $K\alpha$ spectrum of manganese taken from Experiment 2. (*b*) The percentage σ_{se} map, showing a significant improvement in the data quality.

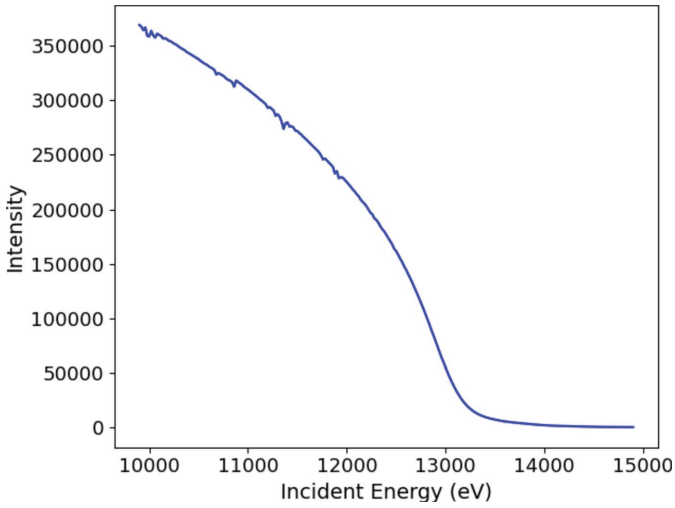

Figure 25
The reflection intensity of the rhodium strip harmonic rejection mirror positioned at an angle of 5.0 mrad as a function of incident energy. Reducing the harmonic cutoff risks introducing harmonic contamination but greatly increases the counts recorded by the upstream ion chamber in the higher energy range.

5. Conclusions

XR-HERFD is a powerful technique, capable of measuring resonant photon scattering processes over an extended range to high accuracy, and it can be used to observe even very low intensity processes with high significance. We have described the key elements and considerations involved in the measurement process from sample preparation to beamline geometry, to optimize measurements for the highest statistics and resolution. Pre-processing and post-processing techniques presented here detail the procedure for observing and removing unwanted systematics from the measurements and reveal the presence of undesired contamination in the sample or beamline path. By taking advantage of the 2D nature of pixel detectors, resolution improvements of up to 54% can be achieved, enhancing the quality of measurements across both incident and emission energy axes. Determination and quantification of data uncertainties and data quality are also detailed, with contributions from additional systematic sources included.

These techniques, whilst specific and tailored to XR-HERFD here, are exactly the same as for a wide range of existing measurement techniques including RIXS and standard HERFD experiments and scans.

Funding information

The following funding is acknowledged: Australian Research Council (award No. 082426).

References

Ankudinov, A. L., Bouldin, C. E., Rehr, J. J., Sims, J. & Hung, H. (2002). *Phys. Rev. B*, **65**, 104107.
Bearden, J. A. (1967). *Rev. Mod. Phys.* **39**, 78–124.
Bearden, J. A. & Burr, F. A. (1967). *Rev. Mod. Phys.* **39**, 125–142.
Bianconi, A. (1980). *Appl. Surf. Sci.* **6**, 392–418.
Blume, M. (1985). *J. Appl. Phys.* **57**, 3615–3618.
Braicovich, L., Ament, L. J., Bisogni, V., Forte, F., Aruta, C., Balestrino, G., Brookes, N. B., De Luca, G. M., Medaglia, P. G., Granozio, F. M., Radovic, M., Salluzzo, M., van den Brink, J. & Ghiringhelli, G. (2009). *Phys. Rev. Lett.* **102**, 167401.
Caliebe, W., Kao, C.-C., Hastings, J., Taguchi, M., Kotani, A., Uozumi, T. & de Groot, F. (1998). *Phys. Rev. B*, **58**, 13452–13458.
Campbell, J. & Papp, T. (2001). *At. Data Nucl. Data Tables*, **77**, 1–56.
Carlisle, J. A., Shirley, E. L., Hudson, E. A., Terminello, L. J., Callcott, T. A., Jia, J. J., Ederer, D. L., Perera, R. C. & Himpsel, F. J. (1995). *Phys. Rev. Lett.* **74**, 1234–1237.
Chantler, C. T. (1992). *J. Appl. Cryst.* **25**, 674–693.
Chantler, C. T. & Bourke, J. D. (2024). *International tables for crystallography*, Vol. I, edited by C. T. Chantler, F. Boscherini & B. A. Bunker, ch. 2.25, pp. 230–269. Wiley.
Chantler, C. T. & Deslattes, R. (1995). *Rev. Sci. Instrum.* **66**, 5123–5147.
Chantler, C. T., Smale, L. F. & Hudson, L. T. (2024). *International tables for crystallography*, Vol. C, edited by T. R. Welberry, ch. 4.2.2, *X-ray Energies*. In the press. Wiley.
Chantler, C. T., Tran, C. Q., Paterson, D., Barnea, Z. & Cookson, D. J. (2000*a*). *X-ray Spectrom.* **29**, 449–458.
Chantler, C. T., Tran, C. Q., Paterson, D., Cookson, D. J. & Barnea, Z. (2000*b*). *X-ray Spectrom.* **29**, 459–466.
Chen, C., Dong, C., Asokan, K., Chen, J., Liu, Y., Guo, J., Yang, W., Chen, Y., Hsu, F., Chang, C. & Wu, M. K. (2011). *Supercond. Sci. Technol.* **24**, 115007.
Dean, J., Melia, H., Chantler, C. & Smale, L. (2019). *J. Phys. B At. Mol. Opt. Phys.* **52**, 165002.
Deslattes, R. D., Kessler, E. G., Indelicato, P., de Billy, L., Lindroth, E. & Anton, J. (2003). *Rev. Mod. Phys.* **75**, 35–99.
Deutsch, M., Gang, O., Hämäläinen, K. & Kao, C. (1996). *Phys. Rev. Lett.* **76**, 2424–2427.
Diamant, R., Huotari, S., Hämäläinen, K., Kao, C. & Deutsch, M. (2000). *Phys. Rev. A*, **62**, 052519.
Diaz-Moreno, S., Amboage, M., Basham, M., Boada, R., Bricknell, N. E., Cibin, G., Cobb, T. M., Filik, J., Freeman, A., Geraki, K., Gianolio, D., Hayama, S., Ignatyev, K., Keenan, L., Mikulska, I., Mosselmans, J. F. W., Mudd, J. J. & Parry, S. A. (2018). *J. Synchrotron Rad.* **25**, 998–1009.
Diaz-Moreno, S., Hayama, S., Amboage, M., Freeman, A., Sutter, J. & Duller, G. (2009). *J. Phys. Conf. Ser.* **190**, 012038.
Eisenberger, P., Platzman, P. M. & Winick, H. (1976). *Phys. Rev. B*, **13**, 2377–2380.
Etalaniemi, V., Hämäläinen, K., Manninen, S. & Suortti, P. (1992). *J. Phys. Condens. Matter*, **4**, 879–886.
Filik, J., Ashton, A. W., Chang, P. C. Y., Chater, P. A., Day, S. J., Drakopoulos, M., Gerring, M. W., Hart, M. L., Magdysyuk, O. V., Michalik, S., Smith, A., Tang, C. C., Terrill, N. J., Wharmby, M. T. & Wilhelm, H. (2017). *J. Appl. Cryst.* **50**, 959–966.
Fritsch, M., Kao, C. C., Hämäläinen, K., Gang, O., Förster, E. & Deutsch, M. (1998). *Phys. Rev. A*, **57**, 1686–1697.
Glans, P., Gunnelin, K., Skytt, P., Guo, J.-H., Wassdahl, N., Nordgren, J., Ågren, H., Gel'mukhanov, F. K., Warwick, T. & Rotenberg, E. (1996). *Phys. Rev. Lett.* **76**, 2448–2451.
Glatzel, P. & Bergmann, U. (2005). *Coord. Chem. Rev.* **249**, 65–95.
Glatzel, P., Bergmann, U., Yano, J., Visser, H., Robblee, J. H., Gu, W., de Groot, F. M., Christou, G., Pecoraro, V. L., Cramer, S. P. & Yachandra, V. K. (2004). *J. Am. Chem. Soc.* **126**, 9946–9959.
Glatzel, P., Harris, A., Marion, P., Sikora, M., Weng, T.-C., Guilloud, C., Lafuerza, S., Rovezzi, M., Detlefs, B. & Ducotté, L. (2021). *J. Synchrotron Rad.* **28**, 362–371.
Groot, F. M. F. de (1996). *Phys. Rev. B*, **53**, 7099–7110.
Gurman, S. J. (1995). *J. Synchrotron Rad.* **2**, 56–63.
Hämäläinen, K., Siddons, D. P., Hastings, J. B. & Berman, L. E. (1991). *Phys. Rev. Lett.* **67**, 2850–2853.

Hayama, S., Boada, R., Chaboy, J., Birt, A., Duller, G., Cahill, L., Freeman, A., Amboage, M., Keenan, L. & Diaz-Moreno, S. (2021). *J. Phys. Condens. Matter*, **33**, 284003.
Hayama, S., Duller, G., Sutter, J. P., Amboage, M., Boada, R., Freeman, A., Keenan, L., Nutter, B., Cahill, L., Leicester, P., Kemp, B., Rubies, N. & Diaz-Moreno, S. (2018). *J. Synchrotron Rad.* **25**, 1556–1564.
Hayashi, H. (2008). *Anal. Sci.* **24**, 15–23.
Hayashi, H., Kawata, M., Takeda, R., Udagawa, Y., Watanabe, Y., Takano, T., Nanao, S. & Kawamura, N. (2004). *J. Electron Spectrosc. Relat. Phenom.* **136**, 191–197.
Henderson, G. S., de Groot, F. M. F. & Moulton, B. J. A. (2014). *Rev. Mineral. Geochem.* **78**, 75–138.
Honkanen, A.-P., Verbeni, R., Simonelli, L., Moretti Sala, M., Al-Zein, A., Krisch, M., Monaco, G. & Huotari, S. (2014). *J. Synchrotron Rad.* **21**, 762–767.
Huotari, S., Vankó, Gy., Albergamo, F., Ponchut, C., Graafsma, H., Henriquet, C., Verbeni, R. & Monaco, G. (2005). *J. Synchrotron Rad.* **12**, 467–472.
Joly, Y., Bunău, O., Lorenzo, J.-E., Galéra, R.-M., Grenier, S. & Thompson, B. (2009). *J. Phys. Conf. Ser.* **190**, 012007.
Kao, C.-C., Caliebe, W., Hastings, J. & Gillet, J.-M. (1996). *Phys. Rev. B*, **54**, 16361–16364.
Kavčič, M., Budnar, M., Mühleisen, A., Gasser, F., Žitnik, M., Bučar, K. & Bohinc, R. (2012). *Rev. Sci. Instrum.* **83**, 033113.
Könnecke, M., Akeroyd, F. A., Bernstein, H. J., Brewster, A. S., Campbell, S. I., Clausen, B., Cottrell, S., Hoffmann, J. U., Jemian, P. R., Männicke, D., Osborn, R., Peterson, P. F., Richter, T., Suzuki, J., Watts, B., Wintersberger, E. & Wuttke, J. (2015). *J. Appl. Cryst.* **48**, 301–305.
Kowalska, J. K., Lima, F. A., Pollock, C. J., Rees, J. A. & DeBeer, S. (2016). *Isr. J. Chem.* **56**, 803–815.
Kraft, S., Stümpel, J., Becker, P. & Kuetgens, U. (1996). *Rev. Sci. Instrum.* **67**, 681–687.
Krause, M. O. & Oliver, J. H. (1979). *J. Phys. Chem. Ref. Data*, **8**, 329–338.
Llopart, X., Campbell, M., San Segundo, D., Pernigotti, E. & Dinapoli, R. (2001). *2001 IEEE nuclear science symposium conference record* (Cat. No. 01CH37310), pp. 1484–1488. IEEE.
Masciovecchio, C., Bergmann, U., Krisch, M., Ruocco, G., Sette, F. & Verbeni, R. (1996). *Nucl. Instrum. Methods Phys. Res. B*, **111**, 181–186.
Moretti Sala, M., Martel, K., Henriquet, C., Al Zein, A., Simonelli, L., Sahle, C., Gonzalez, H., Lagier, M.-C., Ponchut, C., Huotari, S., Verbeni, R., Krisch, M. & Monaco, G. (2018). *J. Synchrotron Rad.* **25**, 580–591.
Newville, M., Ravel, B., Haskel, D., Rehr, J., Stern, E. & Yacoby, Y. (1995). *Physica B*, **208–209**, 154–156.
Platzman, P. & Isaacs, E. (1998). *Phys. Rev. B*, **57**, 11107–11114.
Ponchut, C., Rigal, J.-M., Clément, J., Papillon, E., Homs, A. & Petitdemange, S. (2011). *J. Instrum.* **6**, C01069.
Roy, M., Lindsay, J. D., Louch, S. & Gurman, S. J. (2001). *J. Synchrotron Rad.* **8**, 1103–1108.
Safonova, O. V., Tromp, M., van Bokhoven, J. A., de Groot, F. M., Evans, J. & Glatzel, P. (2006). *J. Phys. Chem. B*, **110**, 16162–16164.
Sier, D., Dean, J. W., Tran, N. T. T., Kirk, T., Tran, C. Q., Mosselmans, J. F. W., Diaz-Moreno, S. & Chantler, C. T. (2024). *IUCrJ*, **11**, 620–633.
Sparks, C. J. (1974). *Phys. Rev. Lett.* **33**, 262–265.
Thomas, T. D. (1984). *Phys. Rev. Lett.* **52**, 417–420.
Thompson, A., Lindau, I., Attwood, D., Liu, Y., Gullikson, E., Pianetta, P., Howells, M., Robinson, A., Kim, K.-J., Scofield, J., Kirz, J., Underwood, J., Kortright, J., Williams, G. & Winick, H. (2009). *X-ray data booklet.* University of California, Berkeley, California, USA.
Timoshenko, J. & Frenkel, A. I. (2019). *ACS Catal.* **9**, 10192–10211.
Tran, N. T. T., Sier, D., Kirk, T., Tran, C. Q., Mosselmans, J. F. W., Diaz-Moreno, S. & Chantler, C. T. (2023). *J. Synchrotron Rad.* **30**, 605–612.
Vatai, E. (1988). *Phys. Rev. A*, **38**, 3777–3780.
Wong, J. (1999). *Reference X-ray spectra of metal foils*. EXAFS Materials, Danville, California, USA.
Zimmermann, P., Peredkov, S., Abdala, P. M., DeBeer, S., Tromp, M., Müller, C. & van Bokhoven, J. A. (2020). *Coord. Chem. Rev.* **423**, 213466.